Impact of the MLC on the MRI field distortion of a prototype MRI-linac

Stefan Kolling

Sydney Medical School, University of Sydney, NSW 2006, Australia

Brad Oborn[a)]

Illawarra Cancer Care Centre (ICCC), Wollongong, NSW 2500, Australia

Paul Keall[b)]

Sydney Medical School, University of Sydney, NSW 2006, Australia

(Dated: 18 September 2013)

Purpose: To cope with intrafraction tumor motion, integrated MRI-linac systems for real-time image guidance are currently under development. The multileaf collimator (MLC) is a key component in every state-of-the-art radiotherapy treatment system, allowing for accurate field shaping and tumor tracking. This work quantifies the magnetic impact of a widely used MLC on the MRI field homogeneity for such a modality.

Methods: The finite element method (FEM) was employed to model an MRI-linac assembly comprised of a 1.0 T split-bore MRI magnet and the key ferromagnetic components of a Varian Millennium 120 MLC, namely the leaves and motors. Full 3D magnetic field maps of the system were generated. From these field maps, the peak-to-peak distortion within the MRI imaging volume was evaluated over a 30 cm diameter sphere volume (DSV) around the isocenter and compared to a maximum pre-shim inhomogeneity of 300 μT. Five parametric studies were performed: (1) The source-to-isocenter distance (SID) was varied from 100 to 200 cm, to span the range of a compact system to that with lower magnetic coupling. (2) The MLC model was changed from leaves only to leaves with motors, to determine the contribution to the total distortion caused by MLC leaves and motors separately. (3) The system was configured in the inline or perpendicular orientation, i.e. the linac treatment beam was oriented parallel or perpendicular to the magnetic field direction. (4) The treatment field size was varied from 0×0 to $20 \times 20\,\mathrm{cm}^2$, to span the range of clinical treatment fields. (5) The coil currents were scaled linearly to produce magnetic field strengths B_0 of 0.5, 1.0 and 1.5 T, to estimate how the MLC impact changes with B_0.

Results: (1) The MLC-induced MRI field distortion fell continuously with increasing SID. (2) MLC leaves and motors were found to contribute to the distortion in approximately equal measure. (3) Due to faster falloff of the fringe field, the field distortion was generally smaller in the perpendicular beam orientation. The peak-to-peak DSV distortion was below 300 μT at SID $\geq$ 130 cm (perpendicular) and SID $\geq$ 140 cm (inline) for the 1.0 T design. (4) The simulation of different treatment fields was identified to cause dynamic changes in the field distribution. However, the estimated residual distortion was below 1.2 mm geometric distortion at SID $\geq$ 120 cm (perpendicular) and SID $\geq$ 130 cm (inline) for a 10 mT/m frequency-encoding gra-

dient. (5) Due to magnetic saturation of the MLC materials, the field distortion remained constant at $B_0 > 1.0\,\mathrm{T}$.

Conclusions: This work shows that the MRI field distortions caused by the MLC cannot be ignored and must be thoroughly investigated for any MRI-linac system. The numeric distortion values obtained for our 1.0 T magnet may vary for other magnet designs with substantially different fringe fields, however the concept of modest increases in the SID to reduce the distortion to a shimmable level is generally applicable.

Key words: MLC, Finite element analysis, Magnetic fields, MRI-linac radiotherapy, MRI field distortion

PACS numbers: 87.61.-c, 87.56.J-, 02.70.Dh,

TABLE I Characteristics of the MRI-guided radiotherapy systems currently under development.

Parameter	**Utrecht**	**Alberta**	**Viewray**	**Australia**
Radiation source	6 MV x-rays	6 MV x-rays	^{60}Co γ-rays	6 MV x-rays
Magnetic field	1.5 T	0.2 T, 0.56 T	0.35 T	1.0 T
Magnet type	Closed	Split	Split	Split
Beam orientation	Perpendicular	Perpendicular and Inline	Perpendicular	Perpendicular and Inline

I. INTRODUCTION

Intrafraction organ motion is one of the major challenges in current radiation therapy treatments. During treatment, both the tumor and organs at risk (OAR) may undergo translation, rotation and deformation, as is well-established in the literature[1–4]. In recent years, considerable progress has been made in the field of image-guided radiation therapy (IGRT) to compensate for these effects[5,6]. The term IGRT is broadly defined and includes techniques which allow only pre- or post-treatment imaging as well as such techniques which can provide real-time image guidance during treatment. The focus of this work is solely on the latter techniques which will be referred to as real-time IGRT and their potential for addressing intrafraction organ motion. Despite the wide variety of different real-time IGRT methods, common shortcomings of all methods are the use of ionising radiation for the imaging, thus contributing extra dose to the patient, and the reliance on internal and/or external surrogates for tracking the tumor motion. In the case of internal surrogates, the implantation of fiducial markers is necessary which is an invasive procedure and not suited for all tumor sites. Furthermore, only the target is tracked, whereas adjacent OARs may also undergo (uncorrelated) motion. The inadequacy of current real-time IGRT techniques to fully address the challenges of intrafraction organ motion has motivated the design of MRI-guided radiotherapy systems as the logical next step (Table I). At present, there are currently two second-generation MRI-linac prototypes being developed (UMC Utrecht[7] and University of Alberta[8]), an MRI-guided ^{60}Co radiotherapy system (Viewray[9]), and our groups own first-generation prototype MRI-linac is under construction (Australia). In these systems, the MRI-based image guidance has a number of advantages compared to existing tumor tracking techniques: MRI is noninvasive, nonionising and produces images of superior

soft-tissue contrast.

Whilst these characteristics in theory make MRI an ideal modality for image guidance, the integration of MRI device and linear accelerator (linac) creates several technical challenges. These can be grouped into two categories: (1) the influence of the MRI on normal linac operation and (2) the influence of the linac on normal MRI operation. In the former case, several studies have investigated the influence of the MRI field on the electron gun[10,11], the waveguide[12] and the MLC[13]. In essence, normal linac operation could be restored with appropriate magnetic shielding[14] or magnetic decoupling of the MRI and linac[15]. In the latter case, various studies exist which looked at the ability to take MRI images of phantoms whilst during linac irradiation[7,16] and investigated the effect of the radiation and RF noise from the linac on the gradient RF coils[17,18]. Recently, a proof-of-concept study for tracking of a 1D pencil-beam navigator[19] and a study on tracking of phantom motion on 2D MRI images[20] have demonstrated that image acquisition is possible with MRI-linac prototypes incorporating an MLC.

However, to the best of our knowledge, the magnetic impact of a ferromagnetic MLC has not been studied and reported in the literature for its impact on the MRI field distortion inside an MRI-linac system. For our first-generation MRI-linac system being constructed at the Liverpool Hospital (Sydney, Australia), a Varian Millenium 120 leaf MLC will be used as the final beam collimation method. Although all ferromagnetic parts of the linac are expected to induce some kind of distortion in the MRI imaging volume, a number of reasons suggests to start with simulating the MLC impact. Firstly, the MLC will be the closest ferromagnetic component to the MRI, and therefore experience the strongest magnetic field. Secondly, unlike for steel parts, the magnetic properties of the tungsten-alloy MLC leaves have not been investigated before and hence acquiring this information will be invaluable. Thirdly, we consider replacing the MLC with a nonferromagnetic version a difficult task. The ferromagnetic binders in the tungsten alloy are essential in the manufacturing process to improve machinability of the leaves, whereas the function of other linac steel parts is mostly structural, i.e. replacing them is simpler and will be done regardless.

In this work, we characterize the impact of a widely used MLC on the field homogeneity of a split-bore MRI magnet suitable for MRI-Linac systems as a function of source-to-isocenter distance, implemented MLC components, linac beam orientation, treatment field size and magnetic field strength.

II. METHODS AND MATERIALS

II.A. Models

II.A.1. Magnet model

A 1.0 T split-bore MRI magnet was modeled in COMSOL Multiphysics™ (Version 4.2a). The magnet model used was that of the design for the Australian MRI-linac prototype being constructed by Agilent Technologies. The magnet is essentially comprised of an actively shielded superconducting 82 cm diameter bore magnet wound in a split-pair configuration. The bore aperture, which is the gap between the two halves of the split-bore magnet, is 50 cm. A key design aspect was to allow two possible linac beam orientations with respect to the MRI magnetic field. In the inline configuration, the treatment beam is oriented parallel to the magnetic field direction; in the perpendicular orientation, the beam is perpendicular to the magnetic field direction. The manufacturer specification for the imaging field of the shimmed magnet are a uniformity in B_z of $< 1\,\mu$T and $< 10\,\mu$T over a 20 cm and 30 cm DSV, respectively. The model is represented in COMSOL by its coil configuration and the values for the coil currents were defined in External Current Density nodes according to the manufacturer specifications. Nonferromagnetic hardware components such as the gradient coils and cryostat were not included in the model. A virtual cylindrical air enclosure with a diameter of 20 m and a length of 20 m along the z-axis was used to surround the device for the definition of boundary conditions. At this distance, magnetic insulation $\vec{n} \cdot \vec{B} = 0$ was enforced, i.e. the assumption that the component of the magnetic field normal to the boundary will have fallen to zero. To investigate the impact of the MLC for different magnetic field strengths, the 1.0 T coil currents were linearly scaled to achieve 0.5 and 1.5 T systems. Although this approach is unlikely to produce optimal fringe fields at these field strengths, it was employed in order to only change one variable at a time. The results at these field strengths should be considered as upper limits for the real MLC induced distortion; with a magnet design optimised by a magnet vendor to produce best possible fringe fields at 0.5 and 1.5 T, lower field distortions could potentially be obtained. However, as there are no readily available split-bore magnet designs at 0.5 and 1.5 T, the linear scaling approach gives a first-order estimate of how the magnetic impact of the MLC changes with field strength.

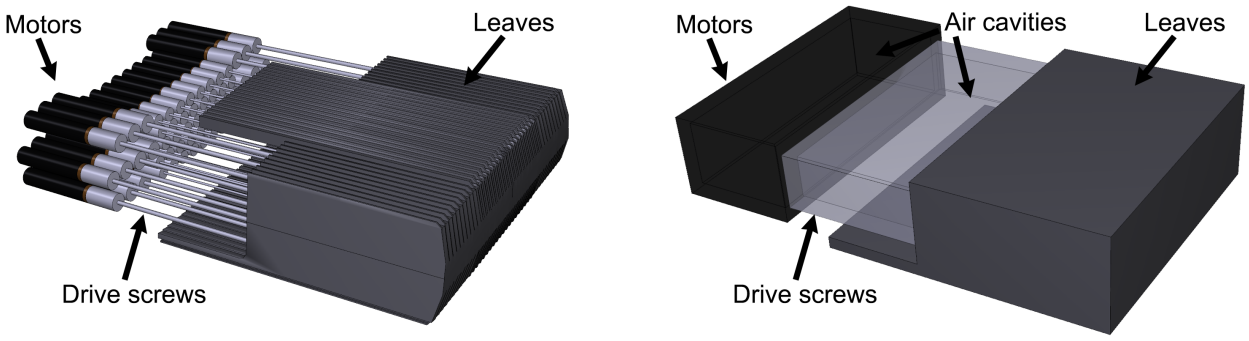

(a) Realistic MLC model

(b) Simplified MLC model

FIG. 1 Implemented model of Varian Millennium 120 MLC. MLC leaves were simplified to rectangular shape and interleaf gaps removed. MLC motors and drive screws are represented through two mass-equivalent steel blocks. Inner air cavities are used to increase the outer extent of the steel blocks to better approximate the real distribution of ferromagnetic material in space.

II.A.2. MLC model

A Varian Millennium 120 MLC (Varian Medical Systems, Palo Alto) was incorporated into the magnet model. Positioned as a tertiary system below the lower jaws, the centroid of the Varian MLC is at a distance of 50.8 cm from the radiation source. This distance varies across vendors, with typically 33.6 cm for Elekta MLC's (positioned as upper jaw replacement) and 33.2 cm for Siemens MLC's (positioned as lower jaw replacement)[21]. Hence, note that for the same SID the Varian MLC is positioned around 17 cm closer to the isocenter than MLC's of the other two vendors. These other MLC devices will also possess different geometry, materials and masses. In this work, the focus is on the Varian Millennium 120 MLC which will be used for our first-generation prototype setup. However, the details about geometry, materials and masses given below will allow to roughly estimate the impact of other MLC devices.

Only the key ferromagnetic components of the MLC were modeled, namely the MLC leaves and motors. The MLC leaves are made from a sintered heavy tungsten alloy, whereas the DC brushed MLC motors comprise of steel casings and drive screws as well as neodymium-iron-boron (NdFeB) rare-earth magnets. To keep simulation of the combined model of MRI magnet and MLC practical, a range of simplifications were made, as shown in Fig. 1. For instance, fine geometric details of the MLC leaves such as rounded leaf tips, steps

and rails were neglected. Interleaf air gaps between adjacent leaves were set to zero and the leaves fused to a single solid to facilitate the meshing of the MLC leaf banks. Fusing of the leaves was the last step in building the MLC model, thereby allowing individual positioning of the leaves beforehand which is needed to simulate the delivery of different treatment fields. Furthermore, the permanent magnets of the motors were not included in the model after a preliminary simulation study confirmed that their impact on the MRI field was of negligible order, i.e. their contribution to the total field inhomogeneity was $< 1\,\%$. Due to their high complexity, the MLC motors and the drive screws were represented by two blocks of their equivalent ferromagnetic mass and the true distribution of ferromagnetic material in space was approximated with the help of inner air cavities (Fig. 1(b)). The outer dimensions of the motor block were $6 \times 20 \times 6\,\mathrm{cm}^3$, whereas the drive-screw block was $14 \times 17 \times 3\,\mathrm{cm}^3$. The dimensions of the inner air cavities were scaled such that all walls of both steel blocks were 0.5 cm thick. In total, the model contained 68 kg of heavy tungsten alloy and 4 kg of steel. Compared to the results of manual measurements on a decommissioned MLC, the model intentionally overestimated the real mass of the MLC components by a safety margin of 7 %. To justify the usage of the mass-equivalent approach, the simplified model of MLC motors and drive screws was compared with a more realistic model of 60 individual motors and drive screws, comprising one half of the MLC (20 full-leaf and 40 half-leaf motors). The latter model implemented the single motors and drive screws as solid structures very similar to Fig. 1(a) but with squared instead of circular cross sections, to achieve better meshing and faster convergence. The 20 full-leaf and 40 half-leaf motors had approximate ferromagnetic masses of 45 g and 30 g, respectively, in the aggregate matching the steel mass of the mass-equivalent model. For this simulation, the two different models of MLC motors and drive screws were placed in a uniform background field of 1.0 T and the agreement of the resulting magnetic field distributions was assessed locally and in the far-field regime.

II.B. Magnetisation curves

The magnetisation (BH) curves used for the simulations are displayed in Fig. 2. The BH curve for the MLC steel parts was based on the curve for 1010 steel as reported in the literature[22,23], whereas the BH curve for the heavy tungsten alloy was measured experimentally from a sample cut from a decommissioned MLC leaf. The exact elemental composition

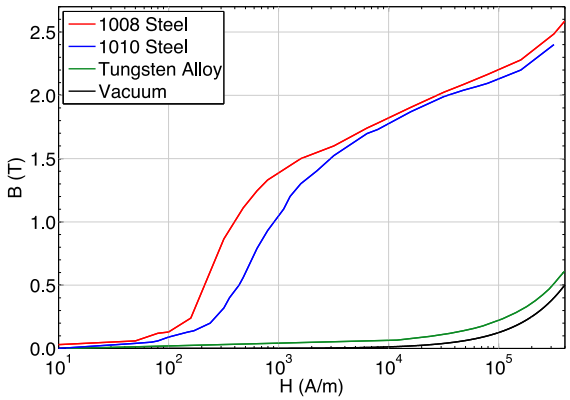

FIG. 2 Magnetisation (BH) curves for the heavy tungsten alloy and 1010 steel, as implemented in the COMSOL model. For comparison, the curves of vacuum and 1008 steel are shown.

of this material is confidential, however it is expected to be similar to the various heavy tungsten alloy grades typically used for radiation shielding which contain $< 10\,\%$ total of a combination of copper, nickel, and iron binders. These additions act to aid the sintering process and machinability.

A Superconducting Quantum Interference Detector (SQUID) magnetometer (Magnetic Property Measurement System 5XL, Quantum Design) was used to determine the BH curve of the heavy tungsten alloy. The measurements were carried out at a temperature of 300 K. Starting with a fully demagnetised sample, the magnetometer measured the magnetic moment induced in the sample of the heavy tungsten alloy as a function of applied external field H in the range of 0 to 8×10^5 A/m. The sensitivity of the magnetometer was 10^{-5} A/m. Data points were acquired with a stepwidth of 4×10^3 A/m in the low-field range from 0 to 8×10^4 A/m; above 8×10^4 A/m, the external field H was increased in bigger steps of 36×10^3 A/m. The magnetic moment was normalised by the sample volume, yielding the volume-independent magnetisation M. For cross-calibration purposes, three samples of the dimensions $3 \times 3 \times 3$, $3 \times 3 \times 4$ and $3 \times 3 \times 6\,\mathrm{mm}^3$ were measured. Then, the magnetic flux density B was derived according to the fundamental relation

$$B(H) = \mu_0(H + M). \tag{1}$$

II.C. Simulations

COMSOL Multiphysics was used to implement the full 3D models of the MRI magnet and MLC components described in Section II.A . Simulations were set up using the Magnetic Fields (mf) interface which is part of the AC/DC Physics module. With the main MRI coil currents being steady over time, the problem could be solved as a magnetostatic problem. Hence, a stationary solver with the magnetic vector potential $\vec{A}$ as the solution variable was chosen. Using the iterative FGMRES solver with the COMSOL default settings, the solution was numerically approximated on the basis of the applicable Maxwell's Equations, namely $\nabla \cdot \vec{B} = 0$ and $\nabla \times \vec{H} = \vec{J}$, where J stands for the electric current densities in the MRI coils. A relative error below 0.001 was defined as the convergence criterion, at which the software terminated the computation and returned a solution.

The nonlinear magnetic permeability of the ferromagnetic materials was incorporated into the COMSOL solution via their respective BH curves (Fig. 2) added under the Material Properties node.

The primary quantity of interest for the data analysis is the magnetic field $\vec{B}$ which was automatically derived within COMSOL from the magnetic vector potential $\vec{A}$ according to the relation $\vec{B} = \nabla \times \vec{A}$.

The FEM mesh used to discretize the geometry was gradually refined until mesh independence was reached for the computed solution. This point was defined by the criterion that further increases in the mesh resolution did not improve the accuracy of the MRI field uniformity evaluated in the 30 cm DSV imaging volume. The final mesh contained a total of 16 million mesh elements, of which 12 million elements were inside a volume of 3 m × 3 m (dia) symmetric cylinder surrounding the MRI coils. The maximum element size within the 30 cm DSV was set to 1.0 cm, giving rise to 2.5 million elements inside the DSV. For the MLC components, the minimum and maximum element sizes were 0.01 and 1.0 cm respectively; the $70 \times 25 \times 10\,\mathrm{cm}^3$ block volume encompassing the MLC structures contained 0.5 million elements.

When solved, a simulation of the bare MRI magnet took around 20 h on 12, 2.6 GHz AMD cores. Adding the MLC leaf banks to the model increased the solution time to around 30 h on the same number of cores; for the full model including the mass-equivalent MLC motors and drive screws, the solution time went further up to around 52 h. The steep increase in

solution time is due to the nonlinearity of the solving process for ferromagnetic objects. The RAM required per simulation was in the range of $180 - 250$ GB.

In both the inline and perpendicular configuration, simulations were performed for a range of SID's as the principal parameter of investigation. Starting from an SID of 100 cm, which is typically used in modern radiotherapy treatment systems, the SID was gradually increased in steps of 5 cm up to a maximum value of 200 cm, thus moving the MLC further away from the MRI magnet.

At each SID, only the MLC leaves were implemented in a first simulation, before the simulation was solved again for the model incorporating both MLC leaves and motors (including the drive screws).

The simulations were repeated at three different magnetic field strengths B_0 of 0.5, 1.0 and 1.5 T. Furthermore, to investigate whether or not active shimming techniques would be necessary, variations in the MRI field homogeneity for different treatment field sizes were studied by simulating field sizes of 0×0, 5×5, 10×10, 15×15 and $20 \times 20\,\mathrm{cm}^2$. Note that the MLC aperture required to achieve a given field size at the isocenter decreases as the MLC and linac are positioned at larger SID. Therefore, the MLC aperture was scaled inversely with increasing SID to keep the field size constant.

II.D. Data analysis

The magnetic field inhomogeneity is typically stated as peak-to-peak distortion over the MRI imaging volume. The shimming for the Australian MRI-linac will be performed by the University of Queensland. Based on recent work, the criterion of 300 μT distortion over a 30 cm DSV has been adopted as the maximum pre-shim inhomogeneity in the 1.0 T system[24]. For each magnetic field simulation, the inhomogeneity in the resultant magnetic flux density $\vec{B}$ was hence analyzed on the surface of the 30 cm DSV around the isocenter in a spherical coordinate system. 28322 datapoints were taken on the DSV surface with an angular resolution of $\Delta\phi = 1.5°$ and $\Delta\theta = 1.5°$. The magnetic field vectors were dominated by the B_z component as the static magnetic field was applied along the z-axis. The concomitant B_x and B_y components were close to zero within the DSV, i.e. below 10^{-6} T, and are generally not considered in shimming. Therefore, the field inhomogeneity was quantified for the B_z component as peak-to-peak distortion, i.e. as the absolute difference (in μT) between the

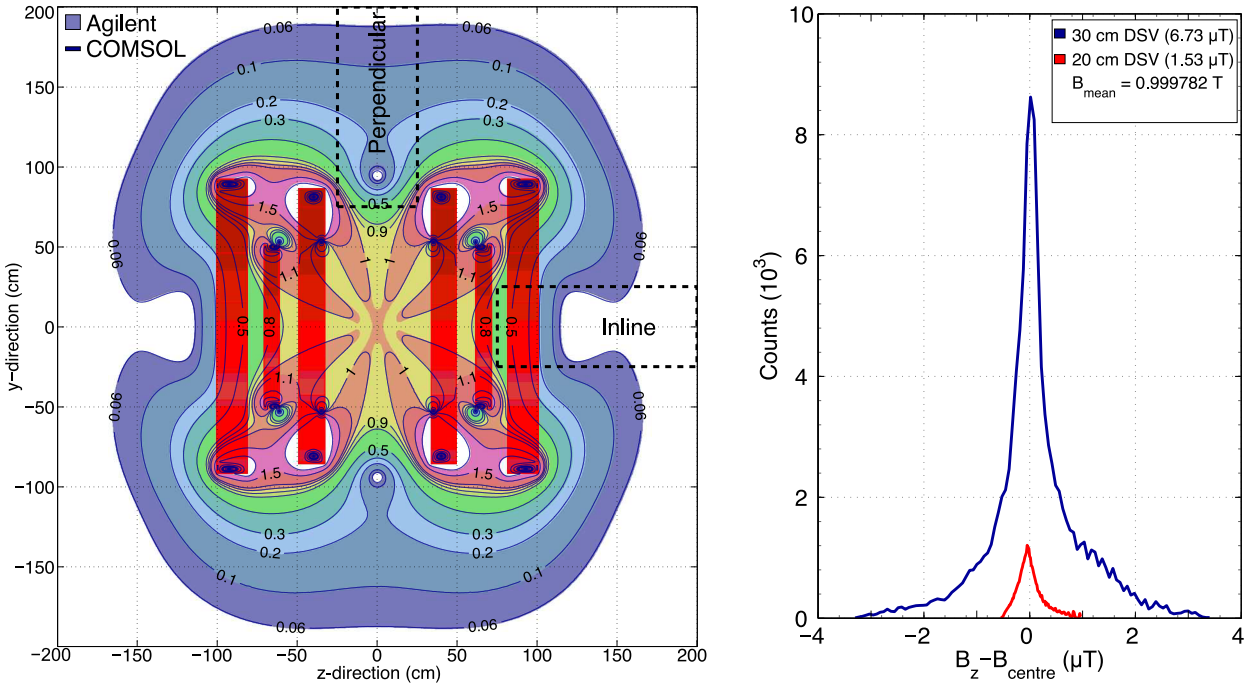

(a)$|\vec{B}|$ field map

(b) DSV uniformity

FIG. 3 (a) Magnetic field magnitude map of the Agilent 1.0 T MRI design (fill plot) and COMSOL match (contour plot). Current coils are shown in red and field values < 0.06 T or > 2 T are shown as white. Our COMSOL results are in excellent agreement with the Agilent data. (b) Histogram of B_z inside the DSV. For the 30 and 20 cm DSV volumes, the spread in B_z is 6.73 and 1.53 μT, respectively. This comfortably matches the manufacturer specification of $< 10\,\mu$T for the 30 cm DSV.

maximum and minimum value of B_z on the DSV surface according to

$$\Delta B_z = B_{z,max} - B_{z,min}. \tag{2}$$

III. RESULTS AND DISCUSSION

III.A. Benchmark magnetic modeling of the MRI design

III.A.1. Model of MRI magnet

Fig. 3(a) shows a magnetic field magnitude ($|\vec{B}|$) plot through the magnet center for the 1.0 T MRI system as obtained by the manufacturer (fill plot). Overlaid on this image

is a contour line plot from our COMSOL model. Two low-field regions are also clearly identified (dashed boxes) and are where the linac and MLC will reside in either the inline or perpendicular configuration. In this plot, regions with a magnitude below 0.06 or above 2.0 T are shown as white. An excellent agreement is seen between the contour and fill plots at selected values between 0.06 and 2.0 T. Only the 1.0 T contour line does not exactly match the Agilent field at the center of the magnet because the mean B_z value within the DSV is 0.999782 T, which is 218 μT lower than 1.0 T. The fact that this is not exactly 1.0 T is not important as all coil currents can be scaled accordingly to get exactly 1.0 T. This procedure is essentially what is done after installation of an MRI system inside a building to correct for magnetization of the surrounding ferromagnetic objects once operational. In our modeling results, we have not scaled the coil currents to get a mean B_z of 1.0 T in the DSV, but decided to keep the coil currents identical to the manufacturer specifications.

In Fig. 3(b), the spectrum of B_z values within the MRI imaging volume obtained for the COMSOL model are displayed. For a 30 cm DSV, the field distortion is 6.8 μT; for the 20 cm DSV, the spread is 1.5 μT. This matches the manufacturer specification for the shimmed magnet of 10 μT over the 30 cm DSV, however is slightly off at 20 cm DSV compared with the specification of 1 μT. Note that a match at the 20 cm DSV can be achieved by further refining the mesh. However, as the distortion is exclusively evaluated over the larger 30 cm DSV throughout this work and the inhomogeneity is higher from 20 to 30 cm than from 0 to 20 cm, increasing the number of mesh elements was not pursued.

It is clear from Fig. 3 that an accurate model of our MRI system has been developed inside COMSOL which matches the manufacturer specifications. Together with the accurate measurement of the BH curve as described in Section II.B, this gives us the ability to predict the impact of the ferromagnetic MLC components on the DSV field homogeneity with high confidence in the next sections.

III.A.2. Model of MLC motors

In a uniform background field of 1.0 T (in B_z direction), the simplified motor model of mass-equivalent blocks was compared with a model of 60 square steel motors. Comparing both models, Fig. 4(a) shows the resultant magnetic field obtained when the MLC motors and their drive screws were placed in this background field. The local field in the proximity

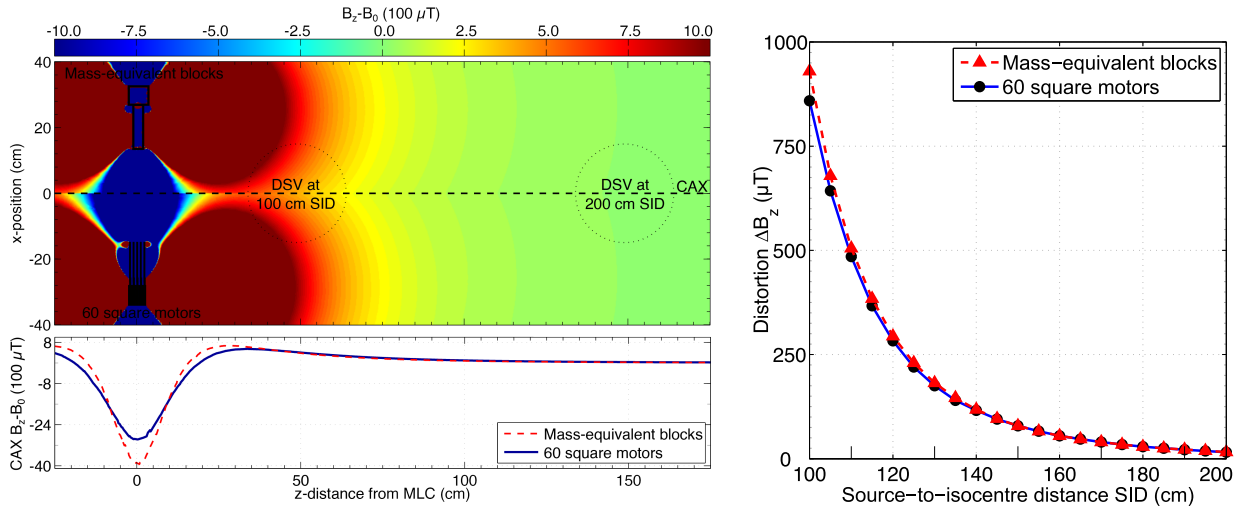

(a) Magnetic field with MLC motors

(b) 30 cm DSV Distortion

FIG. 4 Comparison of the models of mass-equivalent blocks and 60 square motors placed in a uniform 1.0 T (B_0) background field. (a) Top: Field maps are in good agreement in the far-field regime where the DSV distortion is evaluated. Bottom: Magnetic field component B_z along the CAX is shown. (b) Field distortion over 30 cm DSV as a function of SID; for SID $\geq$ 120 cm, the difference between the two models is $< 3\%$.

of the MLC motors is clearly different for the two models since the motor geometry and the distribution of steel strongly influence the field characteristics in this region. However, with increasing distance from the MLC motors, the field distributions become gradually more similar and are in good agreement in the region in which the field distortion is determined for SID's in the range of 100 to 200 cm. Evaluated over a virtual 30 cm DSV, Fig. 4(b) compares the field distortions for both models as a function of distance. At all distances, the simplified model of mass-equivalent blocks with inner air cavities produces a higher inhomogeneity than the model of 60 square motors, with a maximum difference of 8 % at 100 cm SID. Hence, our simplifications can be considered as giving an upper limit for the real field distortion; the difference is below 3 % for SID $\geq$ 120 cm. The mass-equivalent approach was applied throughout the remainder of this work, keeping solving of the simulations feasible.

III.B. MLC bank and motors

For qualitative assessment, Fig. 5 displays B_z in the YZ plane through the isocenter for a series of increasing SID's in the inline (Fig. 5 (a)-(c)) and perpendicular (Fig. 5 (d)-(f)) orientation when only the MLC banks are incorporated in the model. In the inline (perpendicular) orientation, the MLC is positioned in positive z-direction (y-direction). The MLC is implemented in a zero-treatment-field configuration, i.e. the MLC banks are completely closed. This scenario is of particular interest as it represents the default MLC configuration

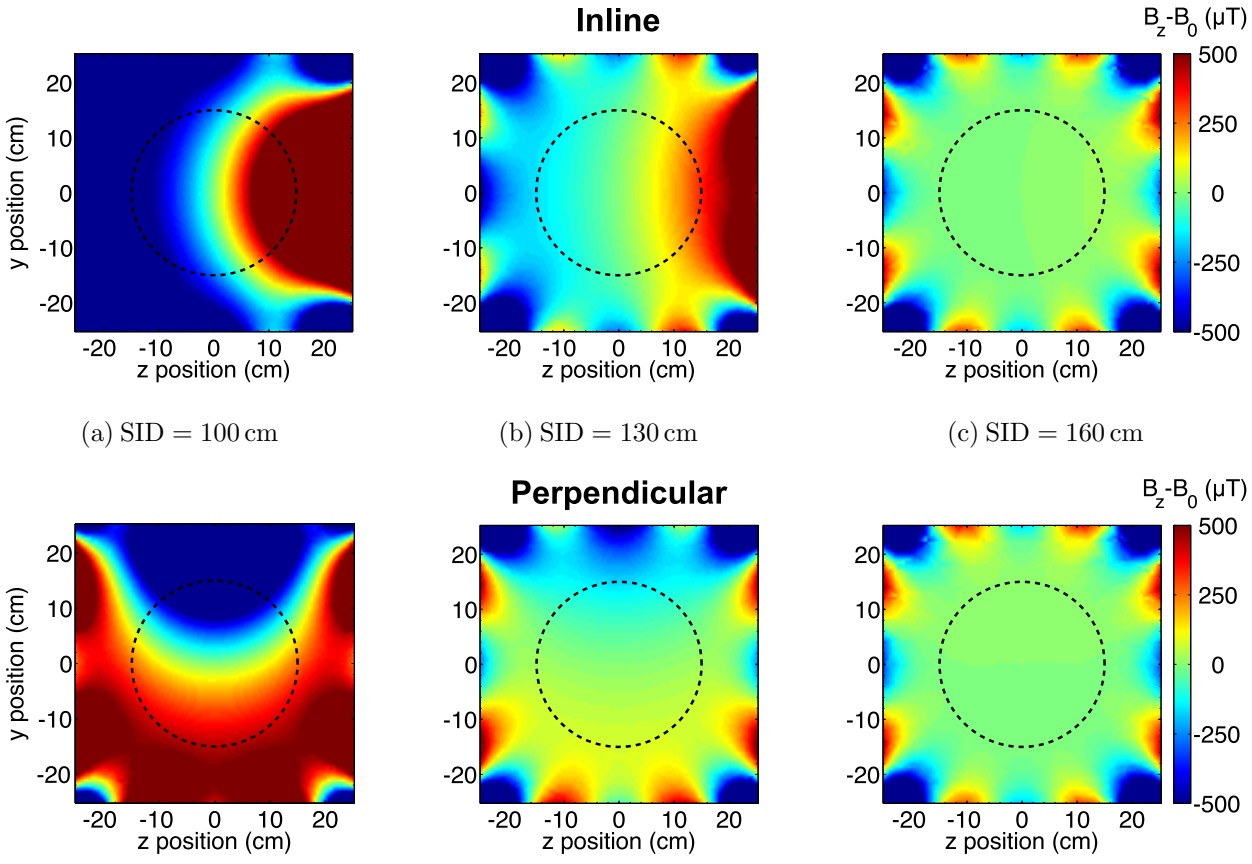

(a) SID = 100 cm (b) SID = 130 cm (c) SID = 160 cm

(d) SID = 100 cm (e) SID = 130 cm (f) SID = 160 cm

FIG. 5 Field imhomogeneity due to the MLC banks for different SID's. The dashed line shows the 30 cm DSV outline. Parts (a)-(c) show the inline orientation; parts (d)-(f) show the perpendicular orientation. In the inline (perpendicular) orientation, the MLC is positioned in positive z-direction (y-direction), gradually lifting B_z from left to right (top to bottom) across the DSV. The field homogeneity improves with increasing SID in both orientations.

before and after treatment. Clearly, the MLC distorts the field homogeneity within the DSV, gradually lifting B_z across the DSV. Qualitatively, the impact of the MLC banks on the MRI field drops continuously with increasing SID.

Fig. 6 extends on these observations showing the quantitative results for both treatment beam orientations. MLC leaves and motors contribute similar orders of magnitude to the total field distortion: The 4 kg of 1010 steel exert approximately the same but slightly higher impact on the DSV field inhomogeneity than the 68 kg of the heavy tungsten alloy comprising the MLC leaves. The total ΔB_z caused by MLC leaves and motors (blue curves in Fig. 6) drops below the pre-shim threshold of 300 μT at 140 cm SID and at 130 cm SID in the inline and perpendicular orientation, respectively. This means that, with respect to the typically used SID of 100 cm, the entire radiotherapy treatment unit must be moved further away from the isocenter by at least 40 cm (inline) or 30 cm (perpendicular).

Comparing the two orientations, the distortion is generally smaller in the perpendicular orientation up to 160 cm SID due to the faster falloff of the fringe field along the y-axis (see Fig. 3(a)). As a consequence of the faster field falloff, B_z drops further below zero in the perpendicular orientation. This higher magnetic fringe field (relative to the inline orientation) gives rise to a slightly higher distortion at SID larger than 160 cm. However, in this SID region, the ΔB_z values are well below 300 μT and therefore uncritical from a shimming perspective in both beam orientations. Worth noting is the particularly low ΔB_z at 145 cm SID in the perpendicular orientation due to the positioning of the MLC in the low-field region around the zero crossing at 95 cm from the isocenter in y-direction for this SID (see Fig. 3(a)).

III.C. Treatment field size

Fig. 7 displays the effect of varying field sizes on the peak-to-peak distortion at a magnetic field strength B_0 of 1.0 T. The plots illustrate that different treatment fields change the distortion patterns during treatment to some extent. The shown changes are solely caused by repositioning of the MLC leaves. MLC motors were neglected in this scenario as they remain stationary during treatment, meaning their unchanged contribution can be shimmed by appropriate passive shimming.

At any given SID, ΔB_z is maximum for the 0×0 cm^2 field and continuously decreases with

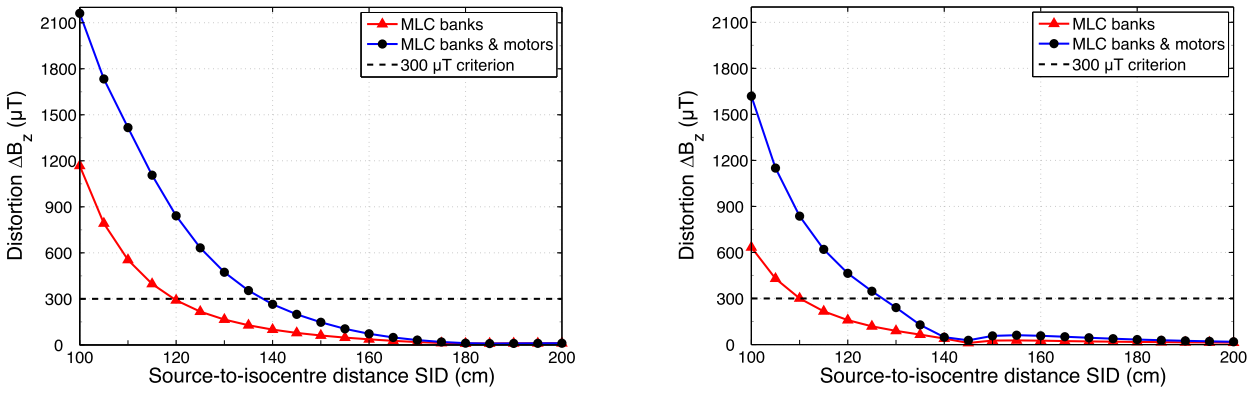

(a) Inline (b) Perpendicular

FIG. 6 Peak-to-peak distortion ΔB_z versus SID. MLC leaves and motors contribute to ΔB_z in similar order. The total ΔB_z (blue curve) lies below 300 μT for SID $\geq$ 140 cm and SID $\geq$ 130 cm in inline and perpendicular orientation, respectively. Due to a steeper falloff of the fringe field, the perpendicular orientation is favorable in terms of field distortion.

increasing field size. As a general trend, the difference in distortion with field size becomes less pronounced for larger SID. This shows that the geometric details of the distribution of ferromagnetic material, such as the exact MLC leaf positions, lose importance with larger distance from the isocenter.

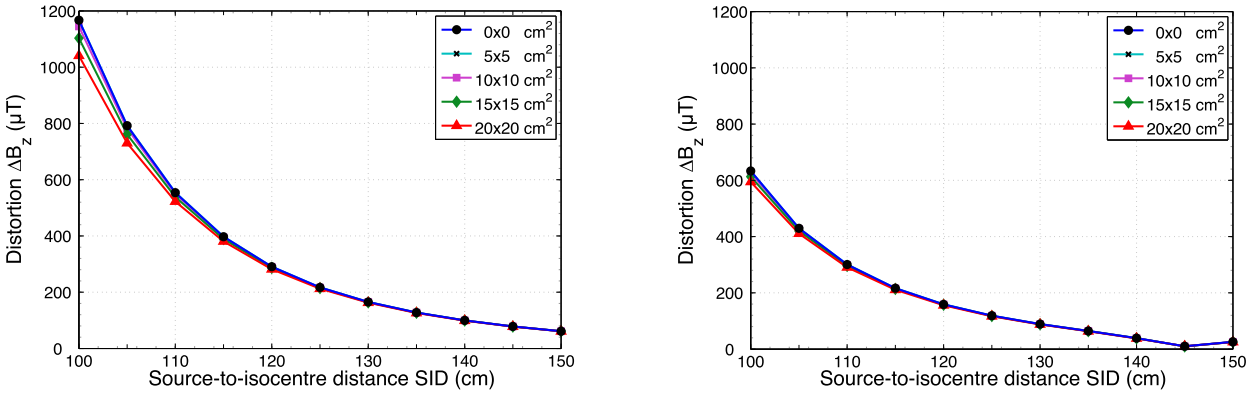

(a) Inline (b) Perpendicular

FIG. 7 Dynamic change in peak-to-peak distortion with treatment field size. Field sizes from 0×0 to $20 \times 20\text{cm}^2$ were simulated. At any given SID, ΔB_z is maximum for the $0 \times 0\,\text{cm}^2$ field and decreases with increasing field size. The differences in ΔB_z caused by the field sizes become smaller with increasing SID, meaning geometric details such as the MLC leaf positions have less impact.

TABLE II Maximum spatial difference in B_z (μT) within 30 cm DSV for various field sizes with respect to $10 \times 10\,\mathrm{cm}^2$ field and B_0 of 1.0 T in (a) inline and (b) perpendicular orientation. Differences are classified as $\leq 2\,\mu$T (green), $\leq 6\,\mu$T (yellow) and $> 6\,\mu$T (red). Based on the use of a 10 mT/m frequency-encoding gradient, these limits together with 10 μT remaining distortion after passive shimming correspond to geometric distortions of ≤ 1.2 mm, when summed linearly (green) or in quadrature (yellow), and > 1.2 mm (red). Geometric distortions up to 1.2 mm can be tolerated for our purposes. Thus, passive shimming may be sufficient for SID ≥ 120 cm (perpendicular) and SID ≥ 130 cm (inline).

(a) Inline

Field	SID (cm)						
(cm^2)	100	110	120	130	140	150	> 150
0x0	37.8	10.4	4.1	2.2	1.8	1.7	
5x5	30.0	6.3	1.8	0.6	0.1	0.1	
10x10	0.0	0.0	0.0	0.0	0.0	0.0	< 1.5
15x15	43.5	11.4	3.4	1.1	0.4	0.2	
20x20	109.8	29.0	8.5	2.9	1.1	0.5	

(b) Perpendicular

Field	SID (cm)						
(cm^2)	100	110	120	130	140	150	> 150
0x0	19.4	6.9	3.4	2.5	2.3	2.0	
5x5	7.7	2.3	0.8	0.3	0.2	0.1	
10x10	0.0	0.0	0.0	0.0	0.0	0.0	< 1.5
15x15	13.1	3.7	1.2	0.6	0.6	0.1	
20x20	32.9	9.4	3.3	1.5	1.6	0.2	

In the following, an optimized passive shim set is assumed for the $10 \times 10\,\mathrm{cm}^2$ field, being in the middle of the spectrum of simulated field sizes. We evaluated in which scenarios this passive shim set produced a sufficiently uniform DSV at the other field sizes, i.e. lead to negligible residual distortions. In the cases where the residual distortion introduced by other field sizes is of an order that cannot be neglected, active shimming is needed to address this extra distortion. In practice, the optimized passive shim set will not completely null the field inhomogeneity but realistically result in a remaining distortion of about 10 μT for the $10 \times 10\,\mathrm{cm}^2$ field. This estimate is in conformity with the manufacturer specification for the DSV field uniformity of the shimmed 1.0 T magnet (II.A.1) and has to be considered together with the residual distortion at other field sizes.

To determine the residual distortion, full 3D analysis of the distortion pattern is required rather than looking at the peak-to-peak distortion. This is necessary as any specific value for the peak-to-peak distortion can be produced by innumerable different 3D field distributions,

each of which needs to be shimmed with a different passive shim set. Thus, for a 3D analysis, the spatial difference in the magnetic field component $B_z(x, y, z)$ is calculated for each field at all SID's with respect to the $10 \times 10\,\mathrm{cm}^2$ reference field and the maximum value within the DSV determined (Table II).

In general, the results for the maximum spatial difference in Table II display the same trends with regards to SID and field size as the peak-to-peak distortion in Fig. 7. The corresponding geometric distortion depends on the strength of the applied frequency-encoding gradient. The proposed 1.0 T system will operate with a gradient strength on the order of $10\,\mathrm{mT/m}$. This means that the $10\,\mu\mathrm{T}$ distortion after passive shimming together with a maximum spatial difference of $2\,\mu\mathrm{T}$ (marked green in Table II) gives rise to 1.2 mm geometric distortion over the 30 cm DSV, which is considered acceptable for our purposes. However, under the assumption of statistical independence, summing the two contributions in quadrature would allow a maximum spatial difference of $6\,\mu\mathrm{T}$ for the same total geometric distortion (yellow). Differences $> 6\,\mu\mathrm{T}$ (red) would require the implementation of active shimming to restore MRI image quality.

Note that the gradient strength may vary in practice. Depending on which particular MRI acquisition sequence is used, the effective gradient strength could be lower. The geometric distortion is proportional to the inverse of the gradient strength and would hence be higher for smaller gradients.

For field sizes up to $20\times20\,\mathrm{cm}^2$, the $6\,\mu\mathrm{T}$ criterion is met for SID $\geq 120\,\mathrm{cm}$ (perpendicular) and SID $\geq 130\,\mathrm{cm}$ (inline). In Section III.B, the closest realisable SID's meeting the $300\,\mu\mathrm{T}$ criterion were found to be 130 cm (perpendicular) and 140 cm (inline). For these SID's, the sole use of passive shimming is sufficient according to Table II. Thus, the implementation of active shimming techniques can be avoided.

III.D. Magnetic field strength

Fig. 8 displays the peak-to-peak distortion versus the SID for magnetic field strengths B_0 of 0.5, 1.0 and 1.5 T. The model contained all MLC components, with the MLC bank in a completely closed configuration ($0 \times 0\,\mathrm{cm}^2$ field size). Other field sizes were not considered here; the distortion values are absolute and not normalized to a $10 \times 10\,\mathrm{cm}^2$ reference field size as in the previous section.

The plots clearly show that higher magnetic field strength B_0 generally increases the field distortion introduced by the MLC. For example, the distortion is the lowest for 0.5 T, with the 300 μT criterion being met for a 5 cm smaller SID compared with strengths of 1.0 T and 1.5 T in both orientations. However, more interesting here is the onset of magnetic saturation becoming obvious in the data at 1.0 and 1.5 T. The saturation can be explained by a closer examination of the magnetic properties of the implemented ferromagnetic materials (Fig. 2). The heavy tungsten alloy comprising the MLC leaves is saturated well below 0.5 T and hence contributes a similar absolute distortion for all three examined field strengths. The BH curve of the 1010 steel changes from positive to negative curvature between 0.5 and 1.0 T. In consequence of operating in a region of negative curvature, approximately the same absolute distortion is produced above 1.0 T.

From an image guidance point of view, higher magnetic field strength is desirable due to improved signal-to-noise ratio. Therefore, higher B_0 could provide better image quality. With this in mind, image quality could be gained without rendering the shimming of the MRI magnet in the presence of the MLC more difficult at $B_0 > 1.0$ T. However, a variety of problems associated with higher B_0 such as a failure of the MLC motors[13], electron gun operation[10] or a more severe electron return effect[25] would have to be overcome. Furthermore, the presented results were derived from scaled coil currents (see Section II.A.1). The applicability of this to a technically feasible model of 1.5 T or higher field strength would have to be investigated in future work.

IV. CONCLUSION

In this work, the finite element method was used to predict the magnetic impact of the Varian Millennium 120 MLC on the DSV field homogeneity for a prototype MRI-linac system. The presented studies showed that the MRI field distortion caused by the MLC cannot be ignored and must be thoroughly investigated for any MRI-linac system. In cases where the field distortion is found to be problematic, increases in the SID can be used to reduce the distortion to an acceptable level, meeting the pre-shim inhomogeneity threshold of 300 μT and limiting the geometric distortion to < 1.2 mm after passive shimming. For our particular 1.0 T magnet design, this was achieved at an SID of 130 cm (perpendicular) or 140 cm (inline). Although the numeric results may vary for other magnet designs due to

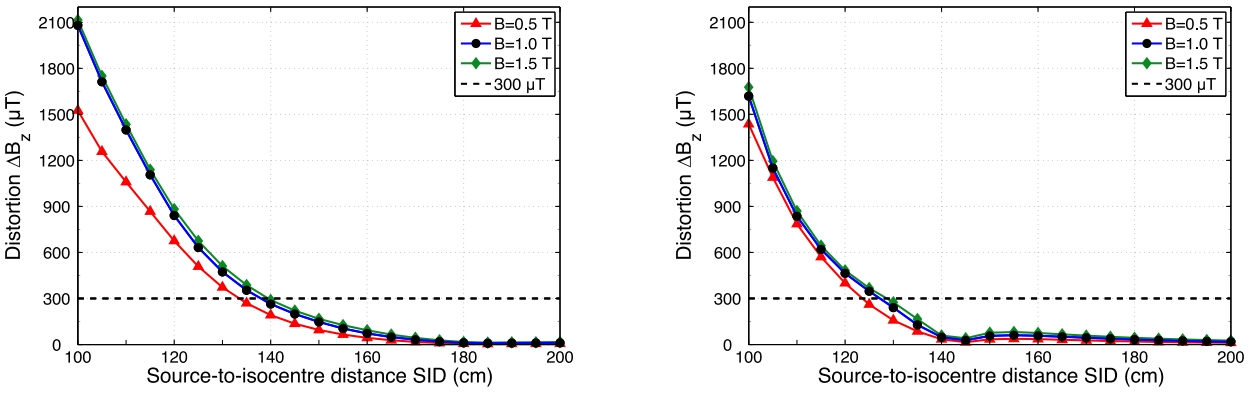

(a) Inline

(b) Perpendicular

FIG. 8 Peak-to-peak distortion ΔB_z versus SID for the MLC in $0 \times 0\,\mathrm{cm}^2$ field configuration and different magnetic field strengths $B_0 = 0.5$, 1.0 and 1.5 T. The saturation of the ferromagnetic materials below 1.0 T results in an almost identical absolute field distortion at magnetic field strengths B_0 of 1.0 and 1.5 T. Thus, a gain in image quality could be obtained without increasing the difficulty of shimming the MRI-linac assembly at 1.5 T.

very different magnetic fringe fields, the concept of modest increases in the SID to reduce the distortion to a shimmable level is generally applicable.

ACKNOWLEDGMENTS

The authors gratefully acknowledge funding through the NHMRC Program Grant 1036078 and ARC Discovery Grant DP120100821. Stefan Kolling wishes to thank the Australian Endeavour Research Fellowship, Studienstiftung des deutschen Volkes and Familie Klee Foundation for financially supporting his work. Further thanks go to Josip Horvat for experimentally determining the BH curves; Stuart Crozier and his group for bringing in their expertise on shimming MRI systems; Uwe Oelfke, Brendan Whelan and Julie Baz for advice and critical feedback.

REFERENCES

[a] Centre for Medical Radiation Physics (CMRP), University of Wollongong, Wollongong, NSW 2500, Australia

[b] Author to whom correspondence should be addressed. E-mail: paul.keall@sydney.edu.au

[1]C. Plathow, M. Schoebinger, C. Fink, H. Hof, J. Debus, H. Meinzer, and H. Kauczor, "Quantification of lung tumor volume and rotation at 3D dynamic parallel MR imaging with view sharing: Preliminary results1," *Radiology*, vol. 240, no. 2, pp. 537–545, 2006.

[2]Y. Suh, S. Dieterich, B. Cho, and P. Keall, "An analysis of thoracic and abdominal tumour motion for stereotactic body radiotherapy patients," *Physics in medicine and biology*, vol. 53, no. 13, p. 3623, 2008.

[3]A. Sawant, K. Pauly, M. Alley, S. Vasanawala, B. Loo, S. Joshi, J. Hinkle, and P. Keall, "Real-time MRI for soft-tissue-based IGRT of moving and deforming lung tumors," *Medical Physics*, vol. 37, p. 3424, 2010.

[4]T. Bortfeld, K. Jokivarsi, M. Goitein, J. Kung, and S. B. Jiang, "Effects of intra-fraction motion on IMRT dose delivery: Statistical analysis and simulation," *Physics in medicine and biology*, vol. 47, no. 13, p. 2203, 2002.

[5]D. Verellen, M. De Ridder, N. Linthout, K. Tournel, G. Soete, and G. Storme, "Innovations in image-guided radiotherapy," *Nature Reviews Cancer*, vol. 7, no. 12, pp. 949–960, 2007.

[6]D. Verellen, M. D. Ridder, and G. Storme, "A (short) history of image-guided radiotherapy," *Radiotherapy and Oncology*, vol. 86, no. 1, pp. 4–13, 2008.

[7]B. Raaymakers, J. Lagendijk, J. Overweg, J. Kok, A. Raaijmakers, E. Kerkhof, R. van der Put, I. Meijsing, S. Crijns, and F. Benedosso, "Integrating a 1.5 T MRI scanner with a 6 MV accelerator: Proof of concept," *Physics in medicine and biology*, vol. 54, no. 12, p. N229, 2009.

[8]B. Fallone, M. Carlone, B. Murray, S. Rathee, T. Stanescu, S. Steciw, K. Wachowicz, and C. Kirkby, "Development of a Linac-MRI System for Real-Time ART," *Medical Physics*, vol. 34, p. 2547, 2007.

[9]J. Dempsey, D. Benoit, J. Fitzsimmons, A. Haghighat, J. Li, D. Low, S. Mutic, J. Palta, H. Romeijn, and G. Sjoden, "A device for realtime 3D image-guided IMRT," *International Journal of Radiation Oncology* Biology* Physics*, vol. 63, pp. S202–S202, 2005.

[10]D. Constantin, R. Fahrig, and P. Keall, "A study of the effect of in-line and perpendicular magnetic fields on beam characteristics of electron guns in medical linear accelerators," *Medical Physics*, vol. 38, no. 7, p. 4174, 2011.

[11]J. S. Aubin, S. Steciw, C. Kirkby, and B. Fallone, "An integrated 6 MV linear accelerator model from electron gun to dose in a water tank," *Medical Physics*, vol. 37, p. 2279, 2010.

[12]J. S. Aubin, S. Steciw, and B. Fallone, "Waveguide detuning caused by transverse magnetic fields on a simulated in-line 6 MV linac," *Medical physics*, vol. 37, p. 4751, 2010.

[13]J. Yun, J. Aubin, S. Rathee, and B. Fallone, "Brushed permanent magnet DC MLC motor operation in an external magnetic field," *Medical Physics*, vol. 37, p. 2131, 2010.

[14]D. Santos, J. S. Aubin, B. Fallone, and S. Steciw, "Magnetic shielding investigation for a 6 MV in-line linac within the parallel configuration of a linac-MR system," *Medical Physics*, vol. 39, p. 788, 2012.

[15]J. Aubin, S. Steciw, and G. Fallone, "Magnetic decoupling of the linac in a low field biplanar linac-MR system," *Medical physics*, vol. 37, p. 4755, 2010.

[16]B. Fallone, B. Murray, S. Rathee, T. Stanescu, S. Steciw, S. Vidakovic, E. Blosser, and D. Tymofichuk, "First MR images obtained during megavoltage photon irradiation from a prototype integrated linac-MR system," *Medical physics*, vol. 36, p. 2084, 2009.

[17]B. Burke, M. Lamey, S. Rathee, B. Murray, and B. Fallone, "Radio frequency noise from clinical linear accelerators," *Physics in medicine and biology*, vol. 54, no. 8, p. 2483, 2009.

[18]B. Burke, A. Ghila, B. Fallone, and S. Rathee, "Radiation induced current in the RF coils of integrated linac-MR systems: The effect of buildup and magnetic field," *Medical Physics*, vol. 39, p. 5004, 2012.

[19]S. Crijns, B. Raaymakers, and J. Lagendijk, "Proof of concept of MRI-guided tracked radiation delivery: tracking one-dimensional motion," *Physics in medicine and biology*, vol. 57, no. 23, p. 7863, 2012.

[20]J. Yun, K. Wachowicz, M. Mackenzie, S. Rathee, D. Robinson, and B. Fallone, "First demonstration of intrafractional tumor-tracked irradiation using 2D phantom MR images on a prototype linac-MR," *Medical physics*, vol. 40, p. 051718, 2013.

[21]J. M. Galvin, "The multileaf collimator: a complete guide," in *Proc. AAPM Annual Meeting*, 1999.

[22]J. R. Brauer, *What Every Engineer Should Know about Finite Elem Anal 2e*, vol. 31. CRC Press, 1993.

[23]Y. Shahbazi, K. Niayesh, and H. Mohseni, "Finite element methode analysis of performance of inductive saturable-core fault current limiter," in *Electric Power Equipment-Switching Technology (ICEPE-ST), 2011 1st International Conference on*, pp. 352–355, IEEE, 2011.

[24]L. Liu, H. Sanchez-Lopez, F. Liu, S. Crozier, *et al.*, "Flanged-edge transverse gradient coil design for a hybrid linac-MRI system," *Journal of Magnetic Resonance*, vol. 226, pp. 70–78, 2013.

[25]A. Raaijmakers, B. Raaymakers, and J. Lagendijk, "Magnetic-field-induced dose effects in MR-guided radiotherapy systems: Dependence on the magnetic field strength," *Physics in medicine and biology*, vol. 53, no. 4, p. 909, 2008.

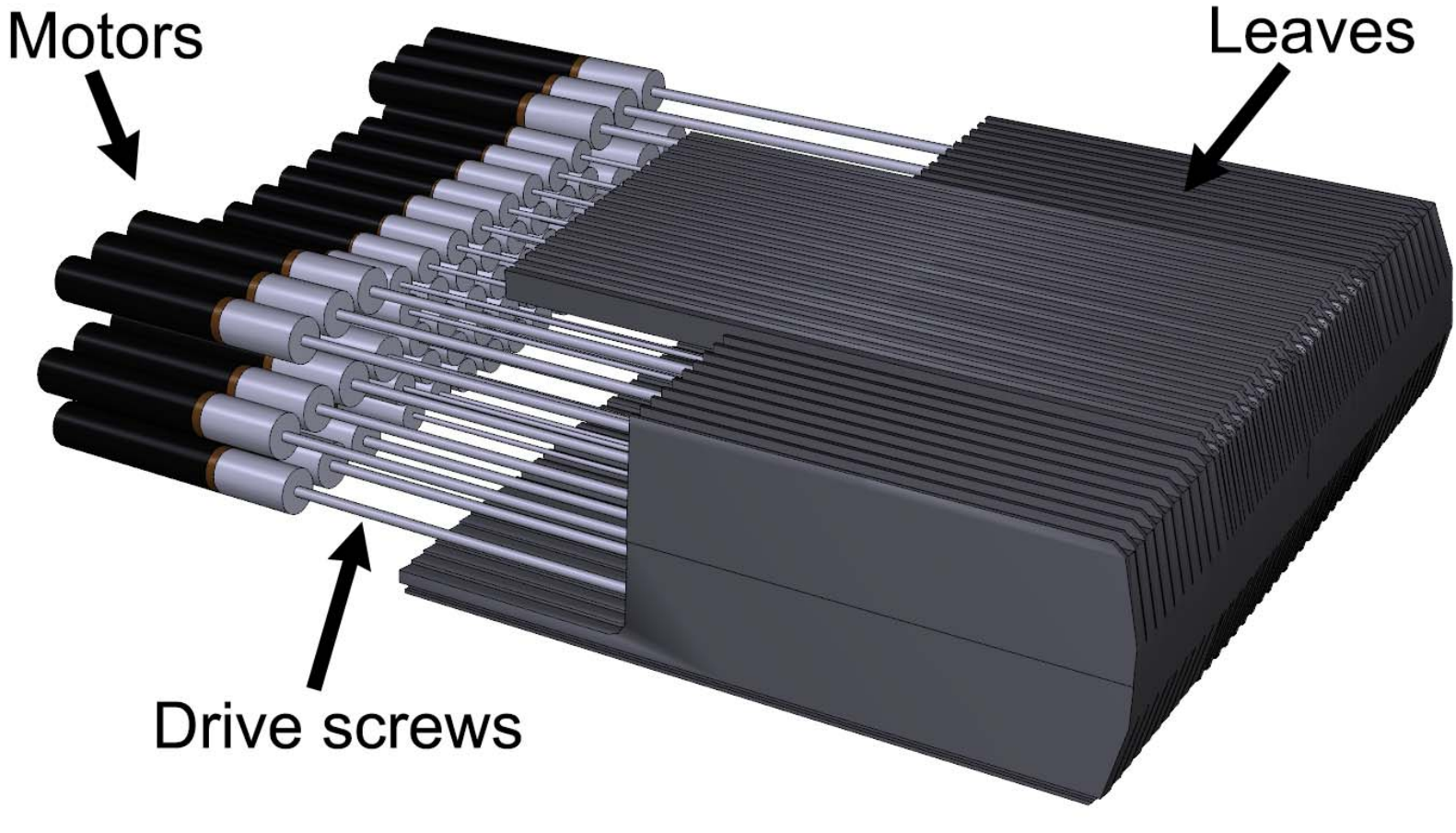
Motors
Leaves
Drive screws

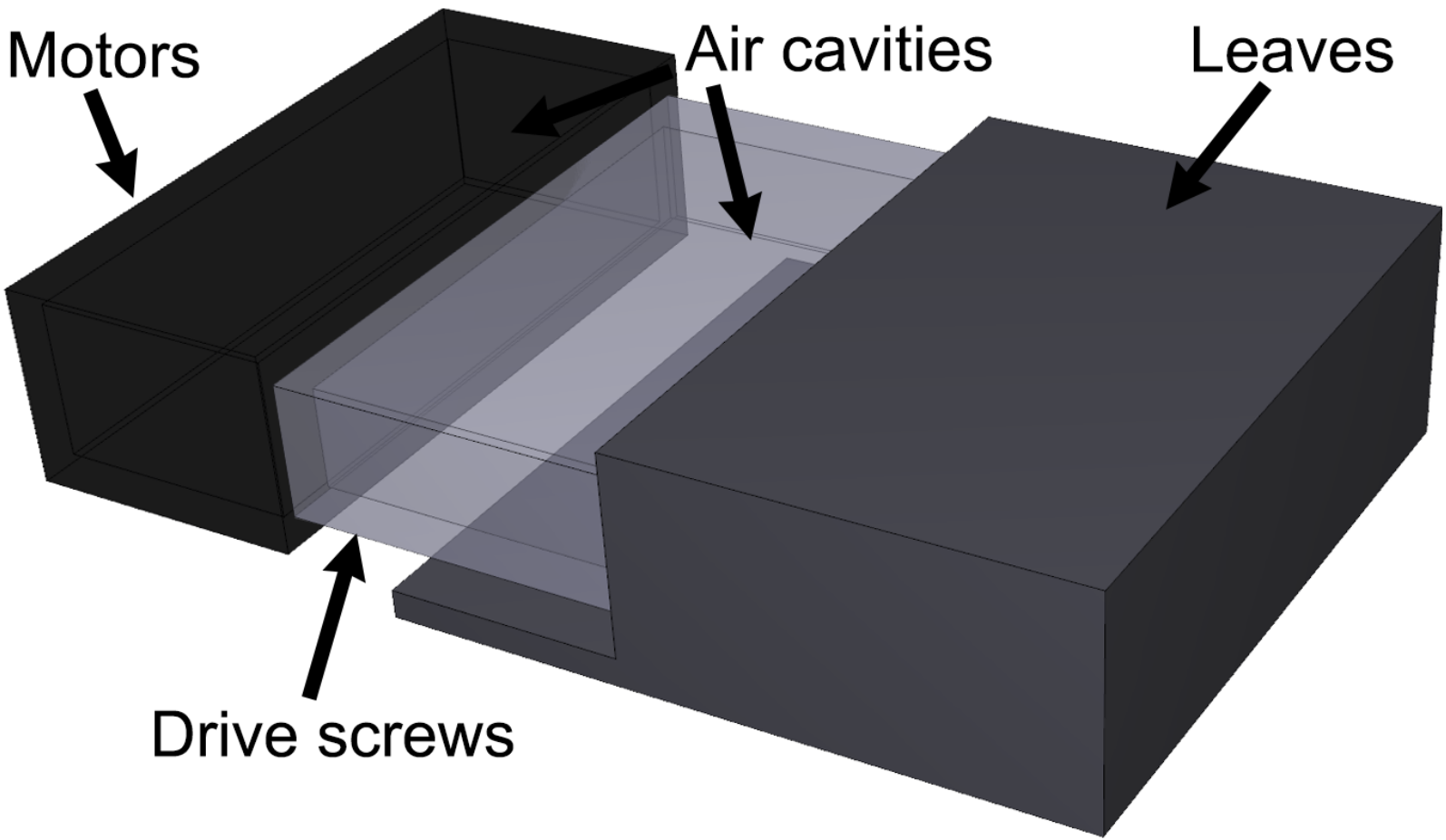
Motors
Air cavities
Leaves
Drive screws

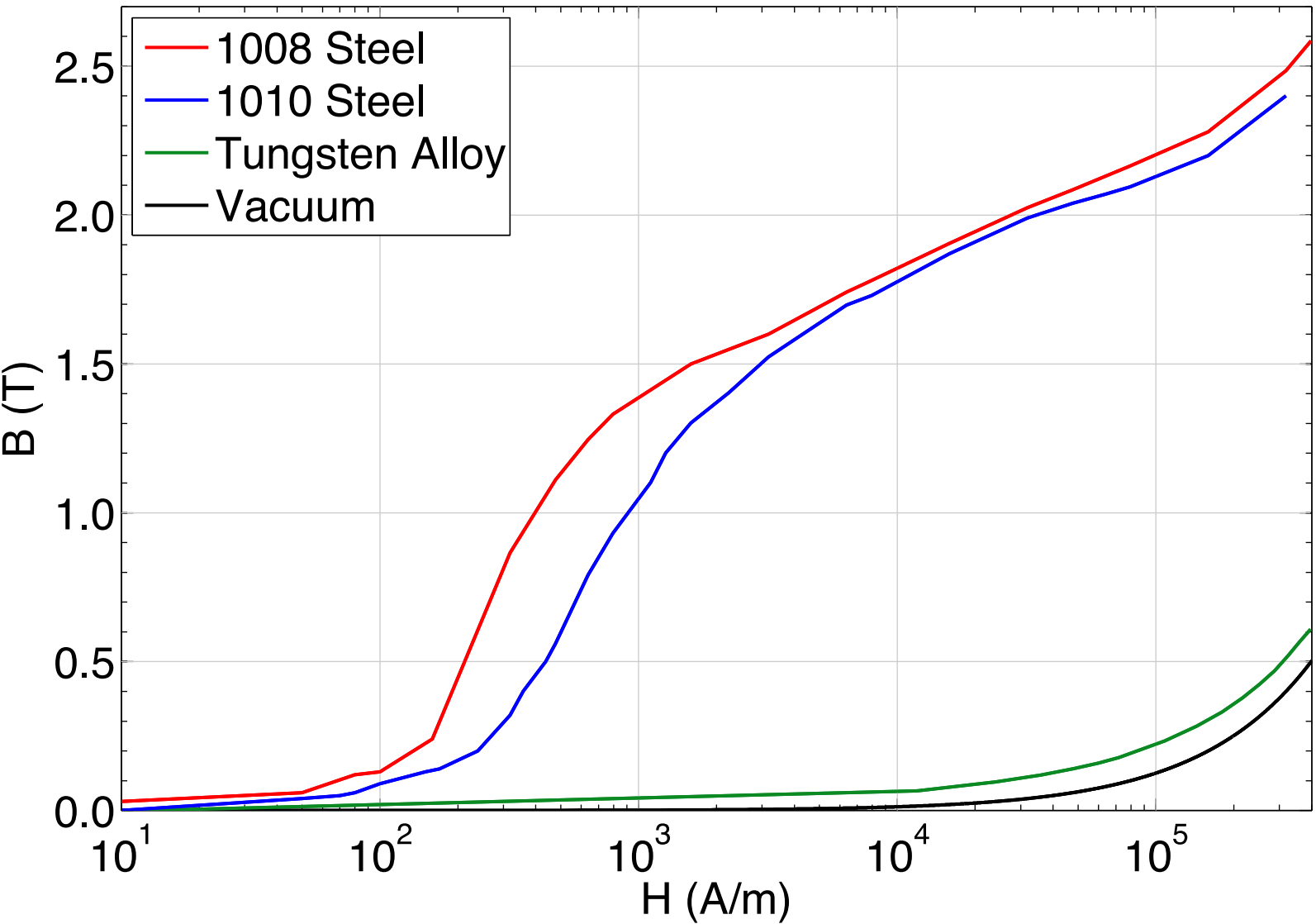
1008 Steel
1010 Steel
Tungsten Alloy
Vacuum
B (T)
2.5
2.0
1.5
1.0
0.5
0.0
10^1
10^2
10^3
10^4
10^5
H (A/m)

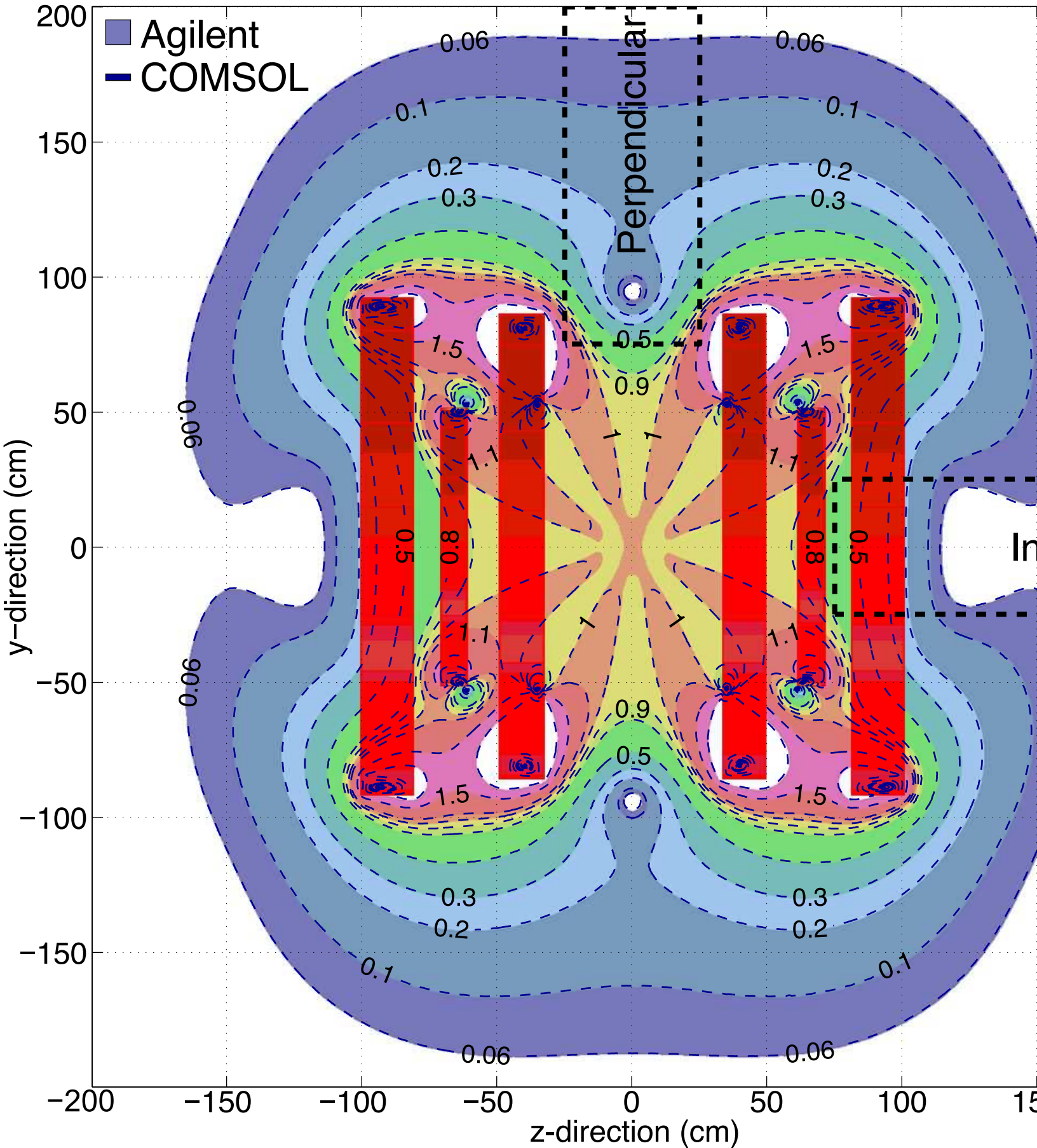
Agilent
COMSOL
Perpendicular
In
0.06
0.1
0.2
0.3
0.5
0.9
1
1.1
1.5
0.8
200
150
100
50
0
−50
−100
−150
−200
−200
−150
−100
−50
0
50
100
y−direction (cm)
z-direction (cm)

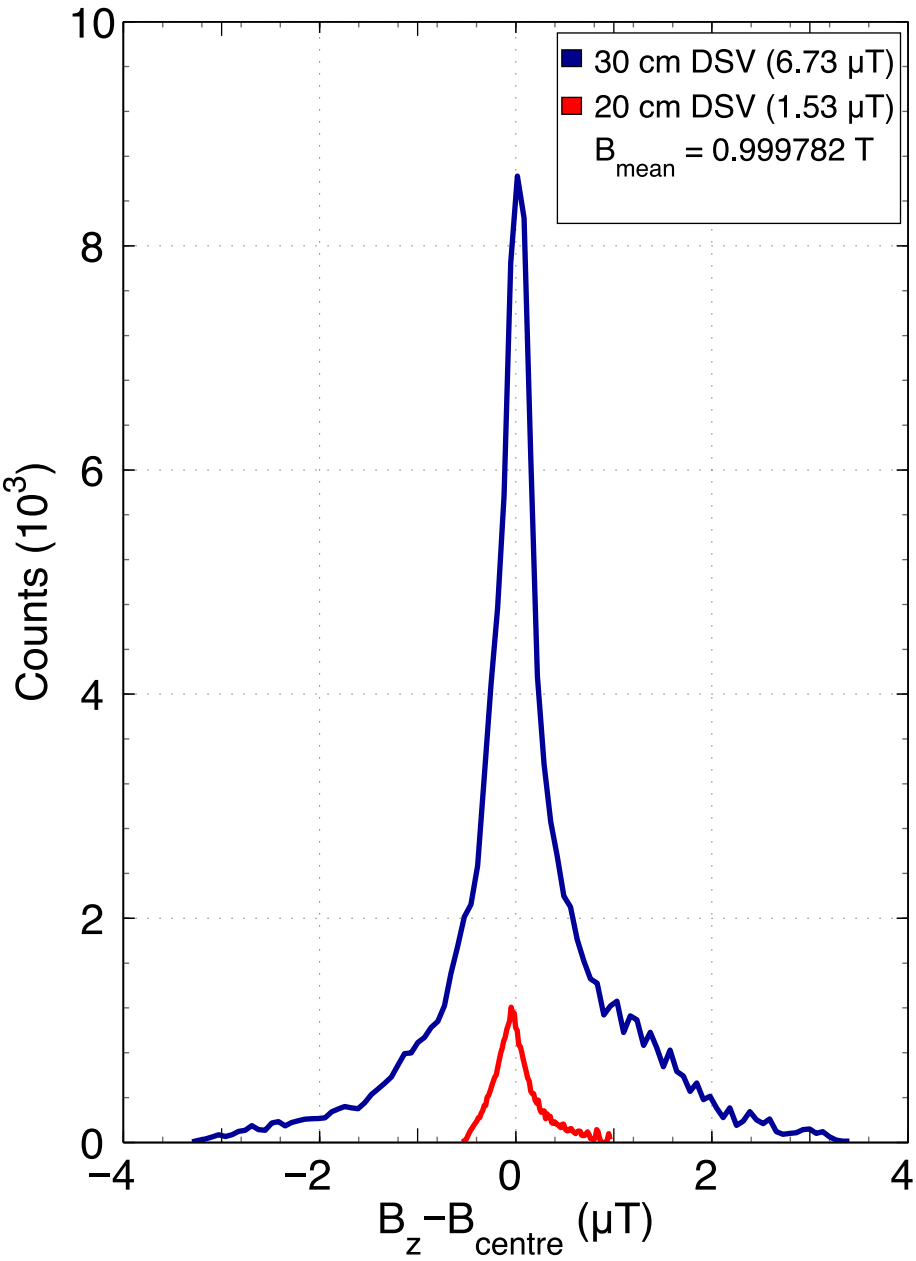
30 cm DSV (6.73 μT)
20 cm DSV (1.53 μT)
B_mean = 0.999782 T
Counts (10^3)
B_z −B_centre (μT)
10
8
6
4
2
0
−4
−2
0
2
4

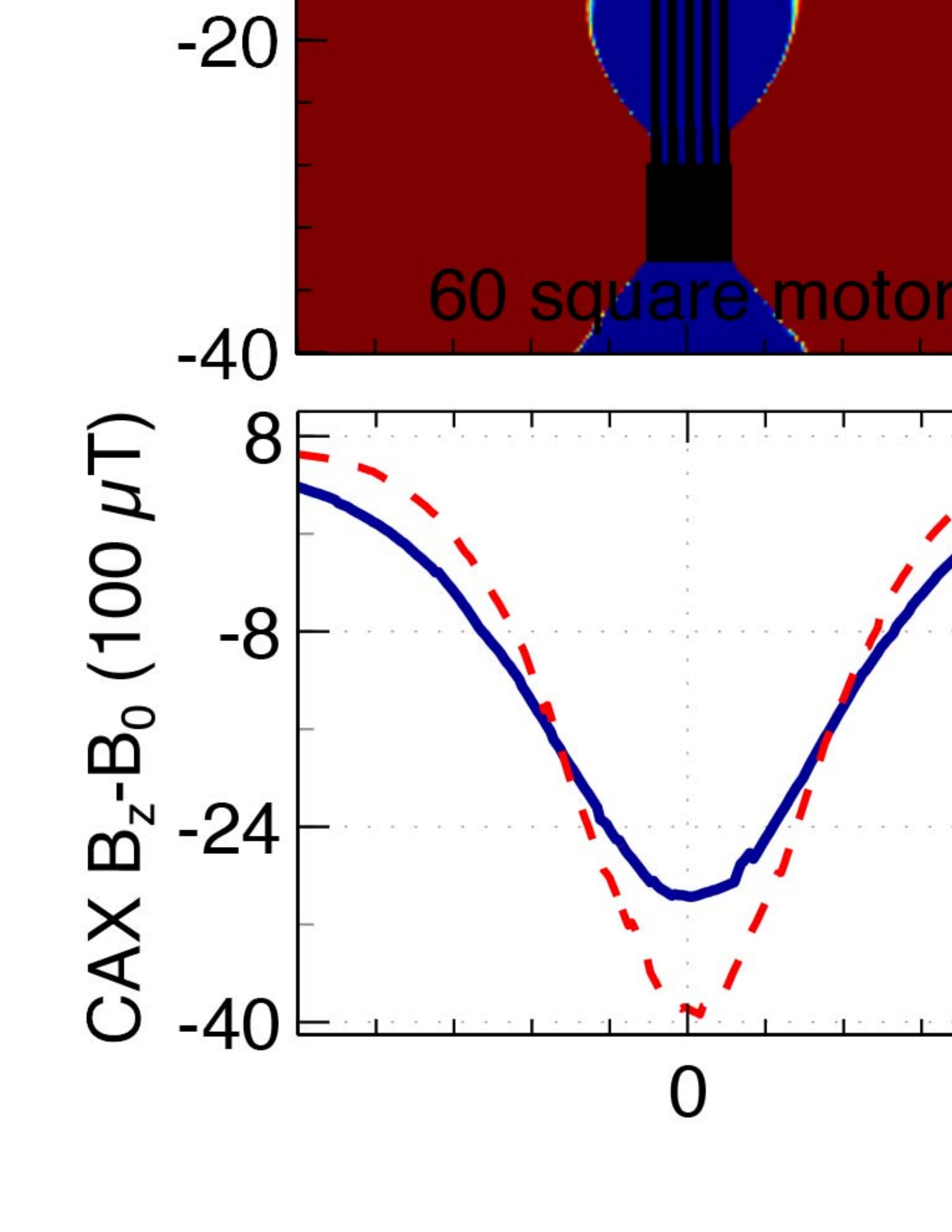
-20
-40
60 square motor
8
-8
-24
-40
CAX B_z-B_0 (100 μT)
0

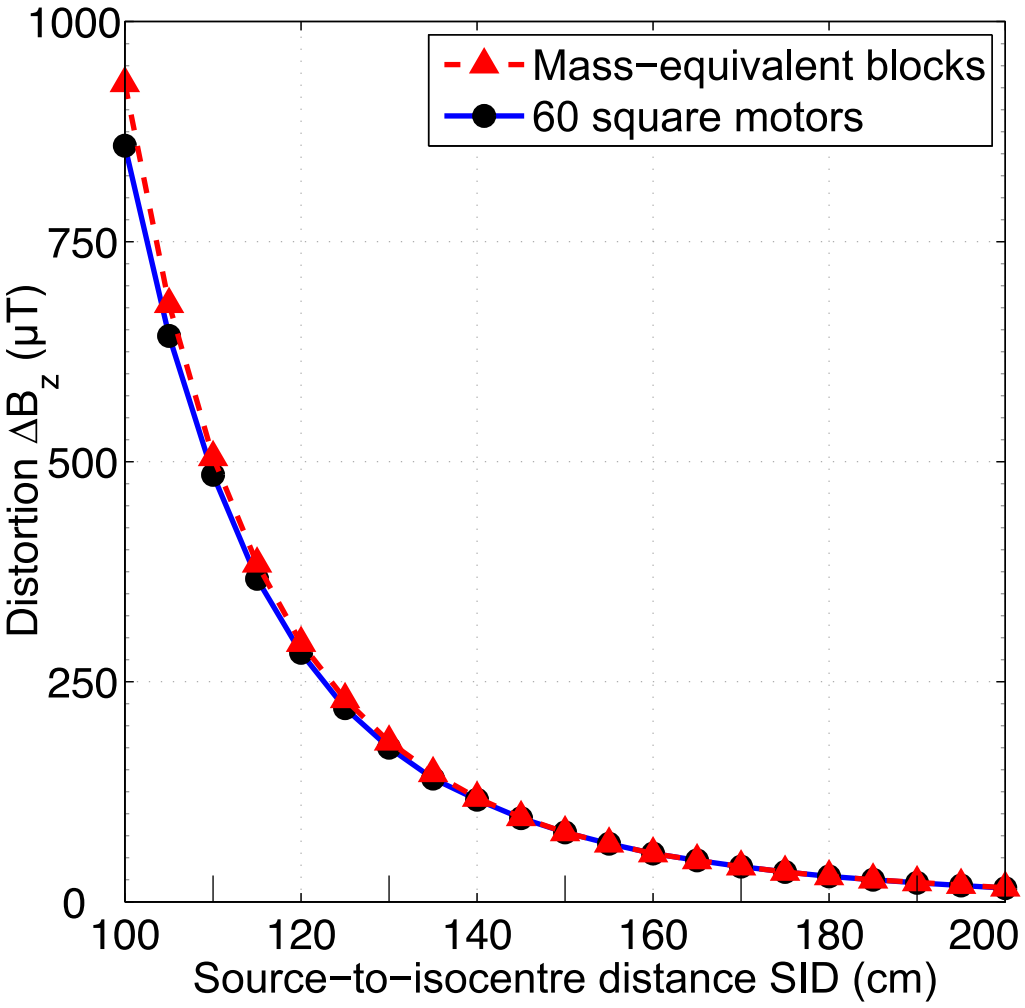
Mass−equivalent blocks
60 square motors
1000
750
500
250
0
Distortion ΔB_z (μT)
100
120
140
160
180
200
Source−to−isocentre distance SID (cm)

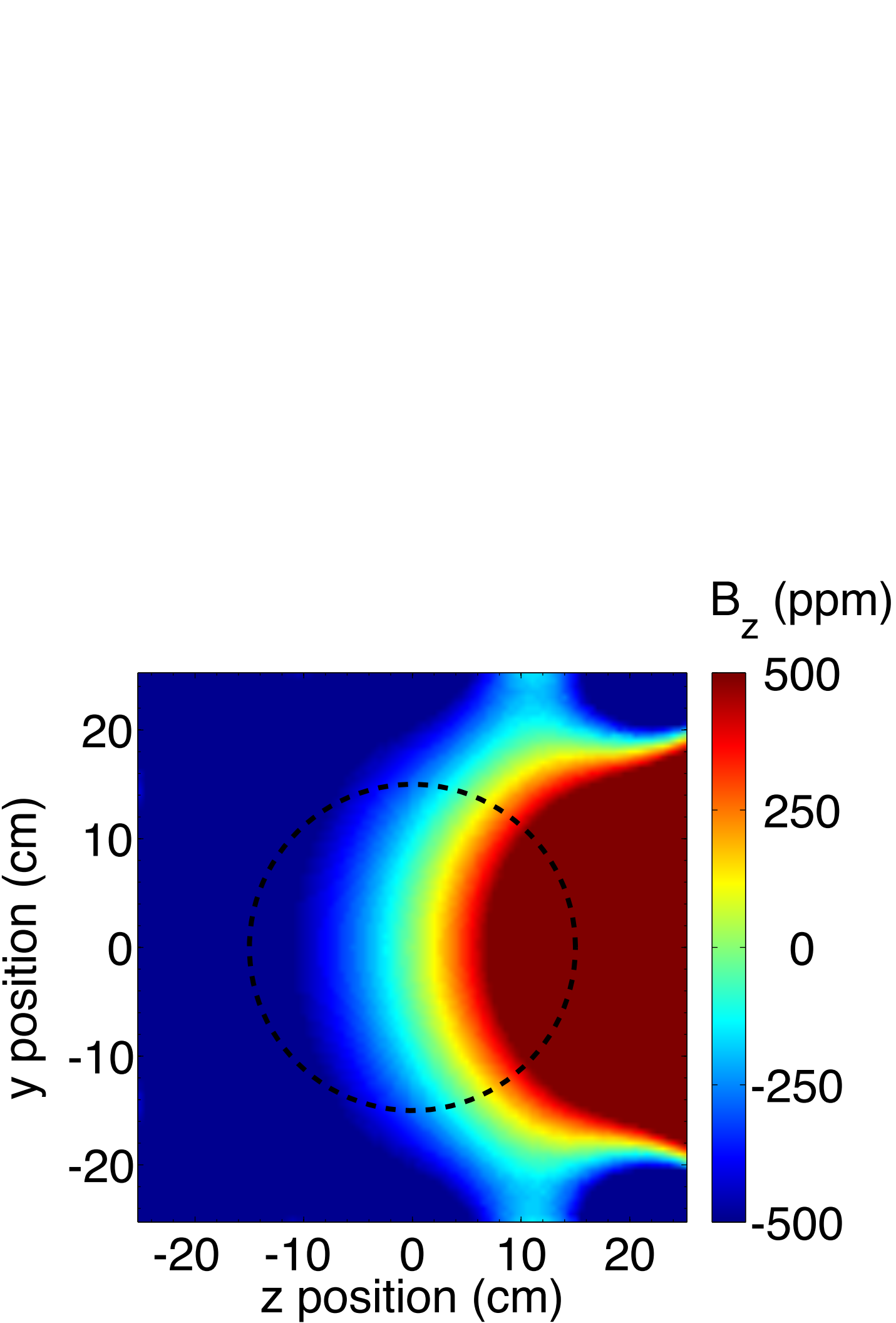
B_z (ppm)
500
250
0
-250
-500
20
10
0
-10
-20
y position (cm)
-20
-10
0
10
20
z position (cm)

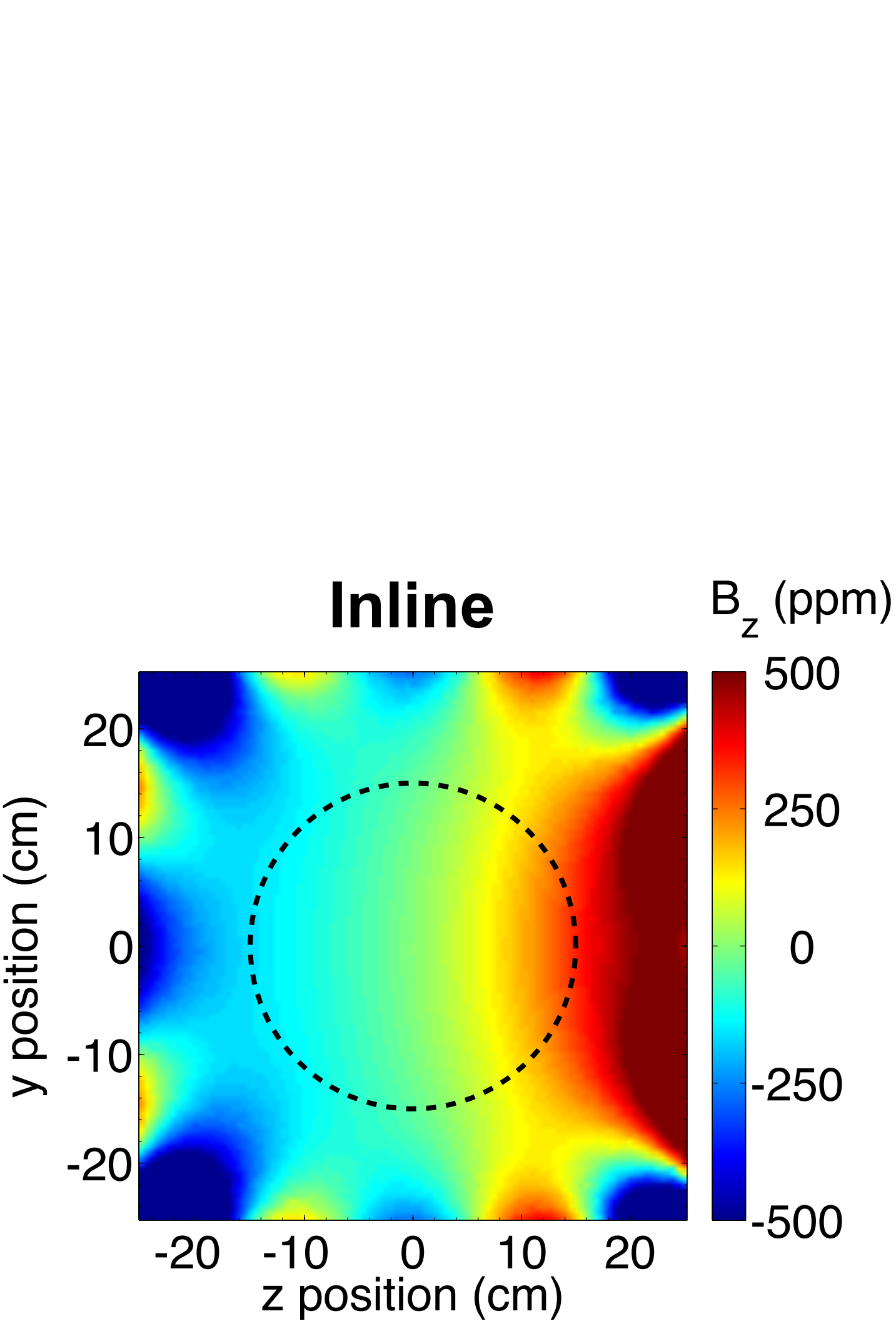
Inline
B_z (ppm)
500
250
0
-250
-500
20
10
0
-10
-20
y position (cm)
-20
-10
0
10
20
z position (cm)

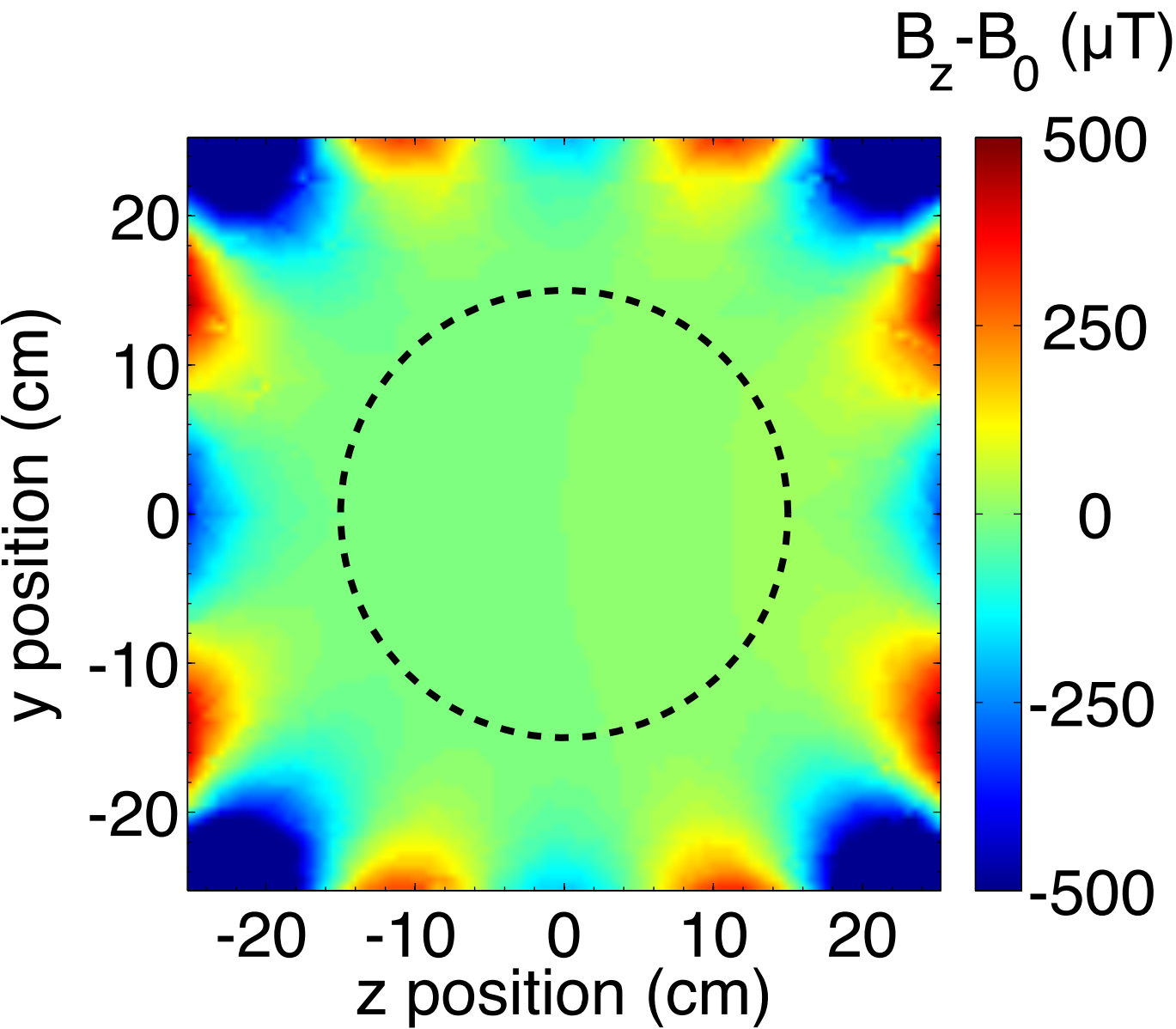
B_z-B_0 (μT)
500
250
0
-250
-500
20
10
0
-10
-20
y position (cm)
-20
-10
0
10
20
z position (cm)

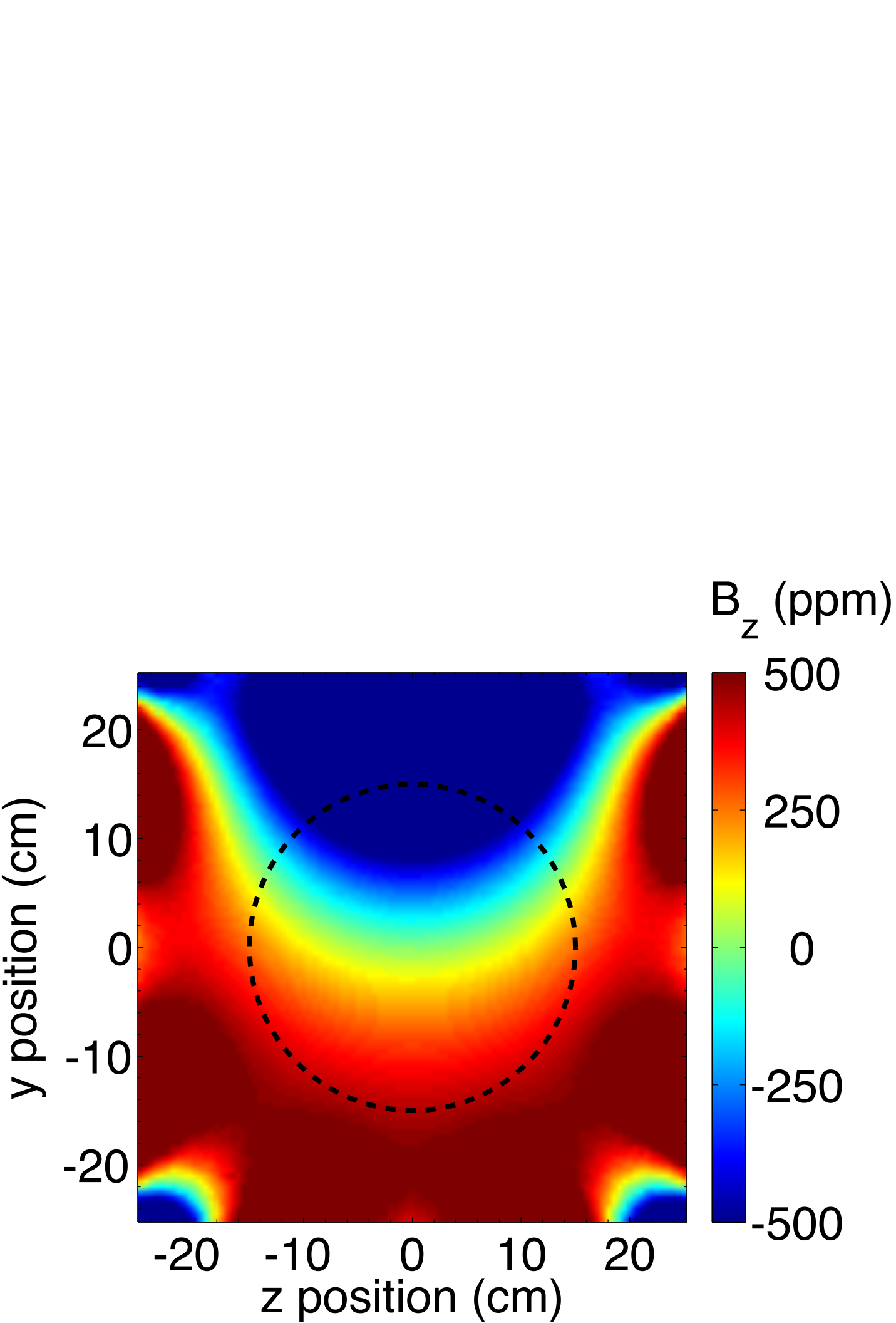
B_z (ppm)
500
250
0
-250
-500
y position (cm)
20
10
0
-10
-20
-20
-10
0
10
20
z position (cm)

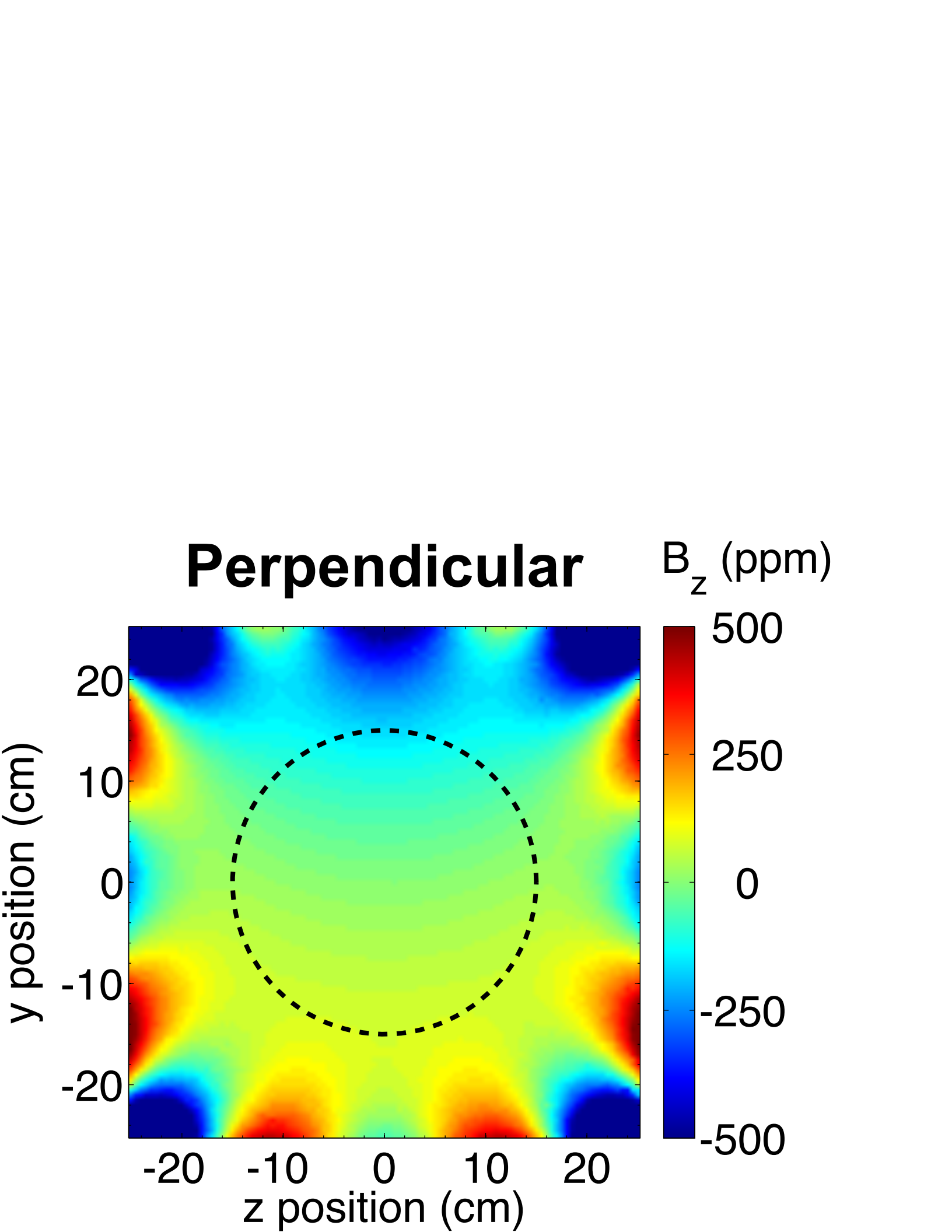
Perpendicular
B_z (ppm)
500
250
0
-250
-500
20
10
0
-10
-20
y position (cm)
-20
-10
0
10
20
z position (cm)

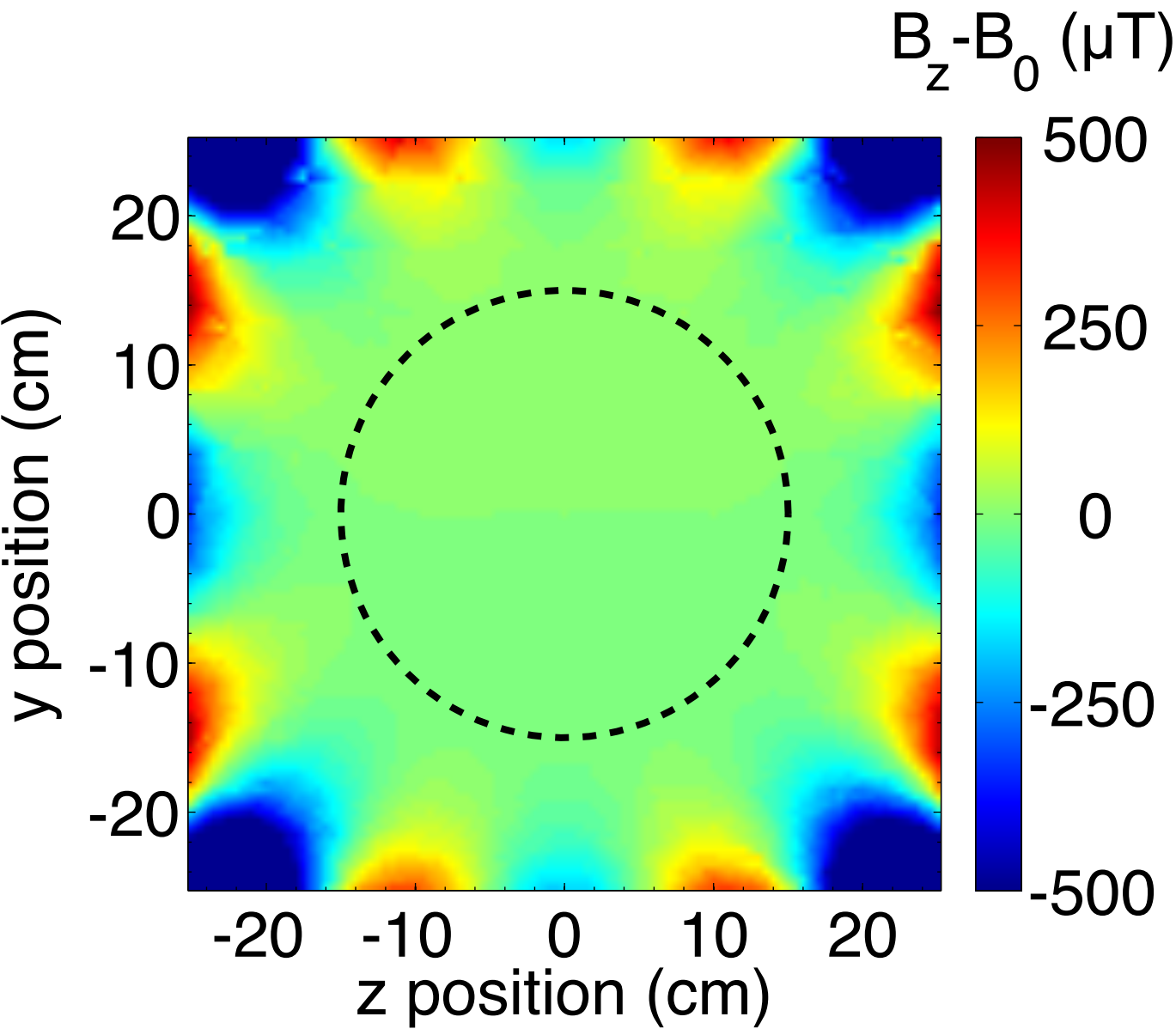
B_z-B_0 (μT)
500
250
0
-250
-500
20
10
0
-10
-20
y position (cm)
-20
-10
0
10
20
z position (cm)

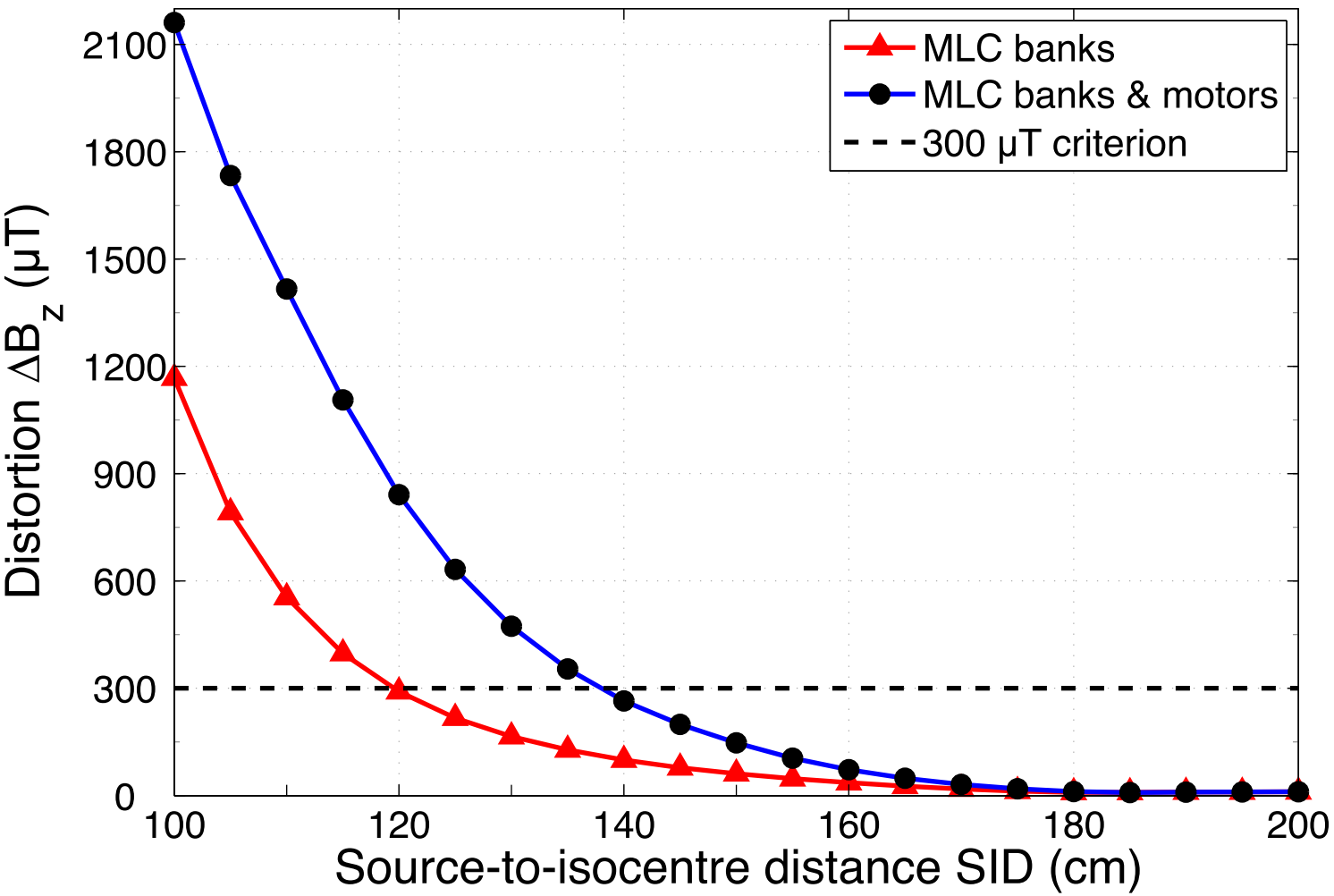
MLC banks
MLC banks & motors
300 µT criterion
2100
1800
1500
1200
900
600
300
0
100
120
140
160
180
200
Distortion ΔB_z (µT)
Source-to-isocentre distance SID (cm)

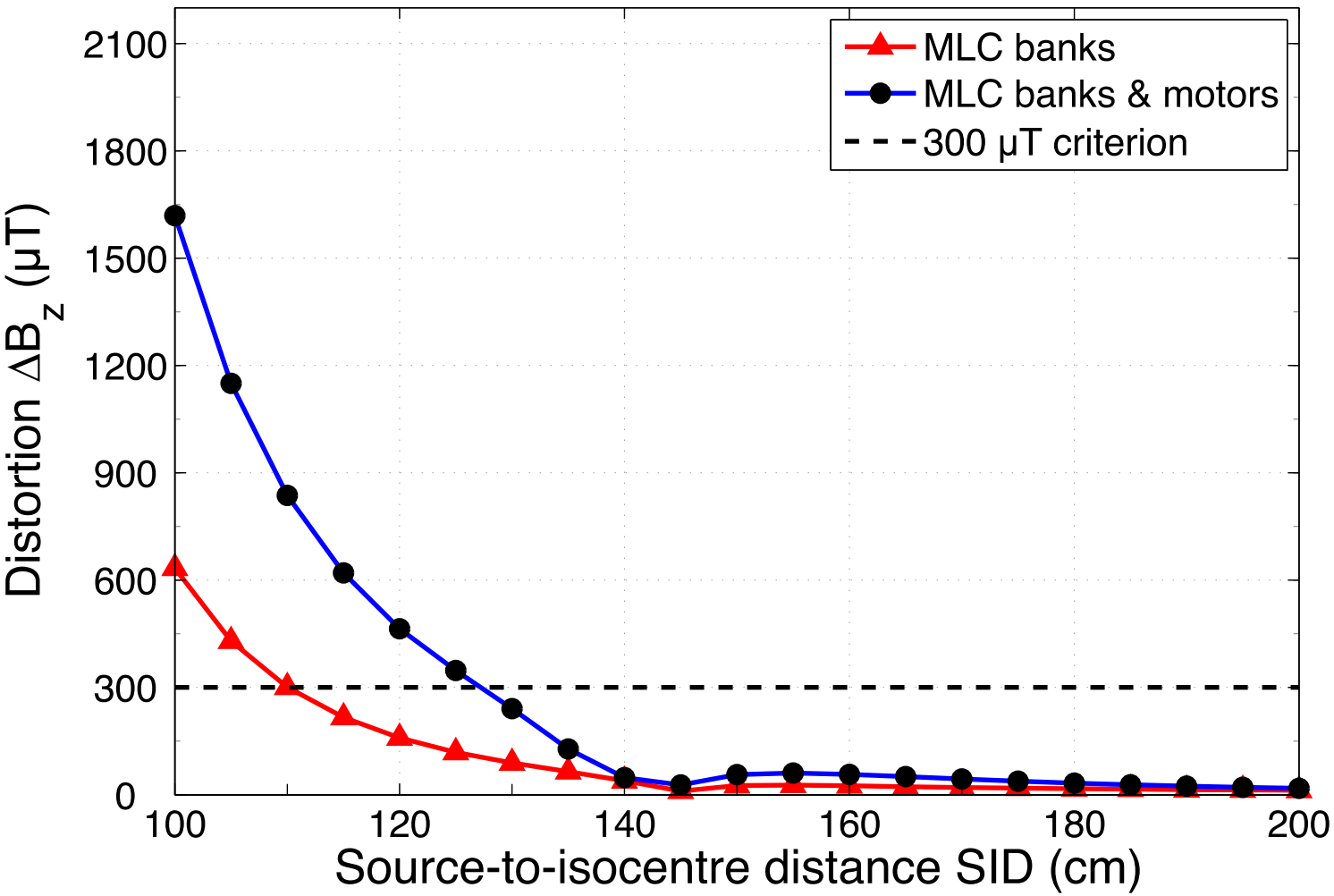
MLC banks
MLC banks & motors
300 µT criterion
2100
1800
1500
1200
900
600
300
0
Distortion ΔB_z (µT)
100
120
140
160
180
200
Source-to-isocentre distance SID (cm)

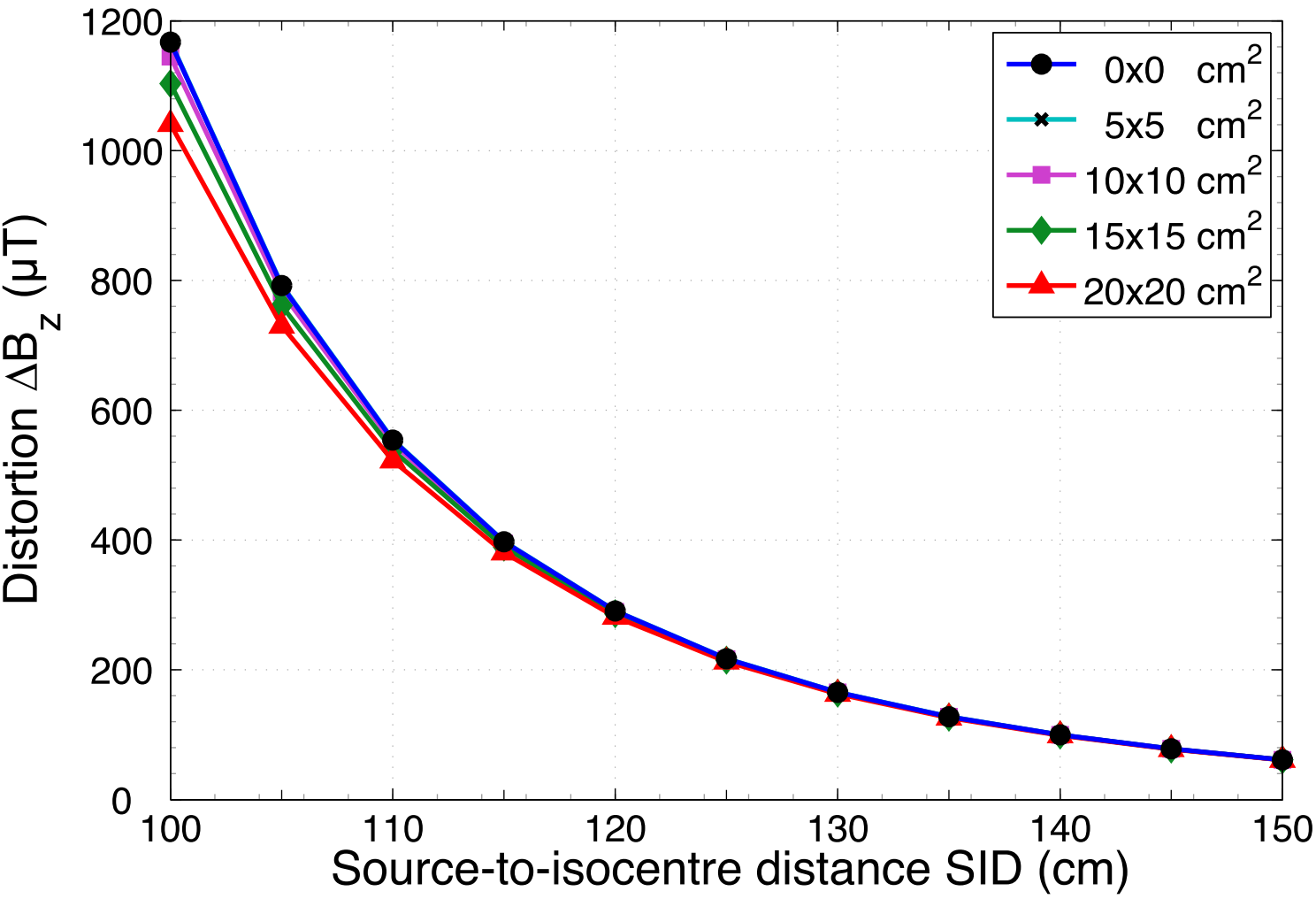
1200
1000
800
600
400
200
0
100
110
120
130
140
150
Distortion ΔB_z (μT)
Source-to-isocentre distance SID (cm)
0x0 cm²
5x5 cm²
10x10 cm²
15x15 cm²
20x20 cm²

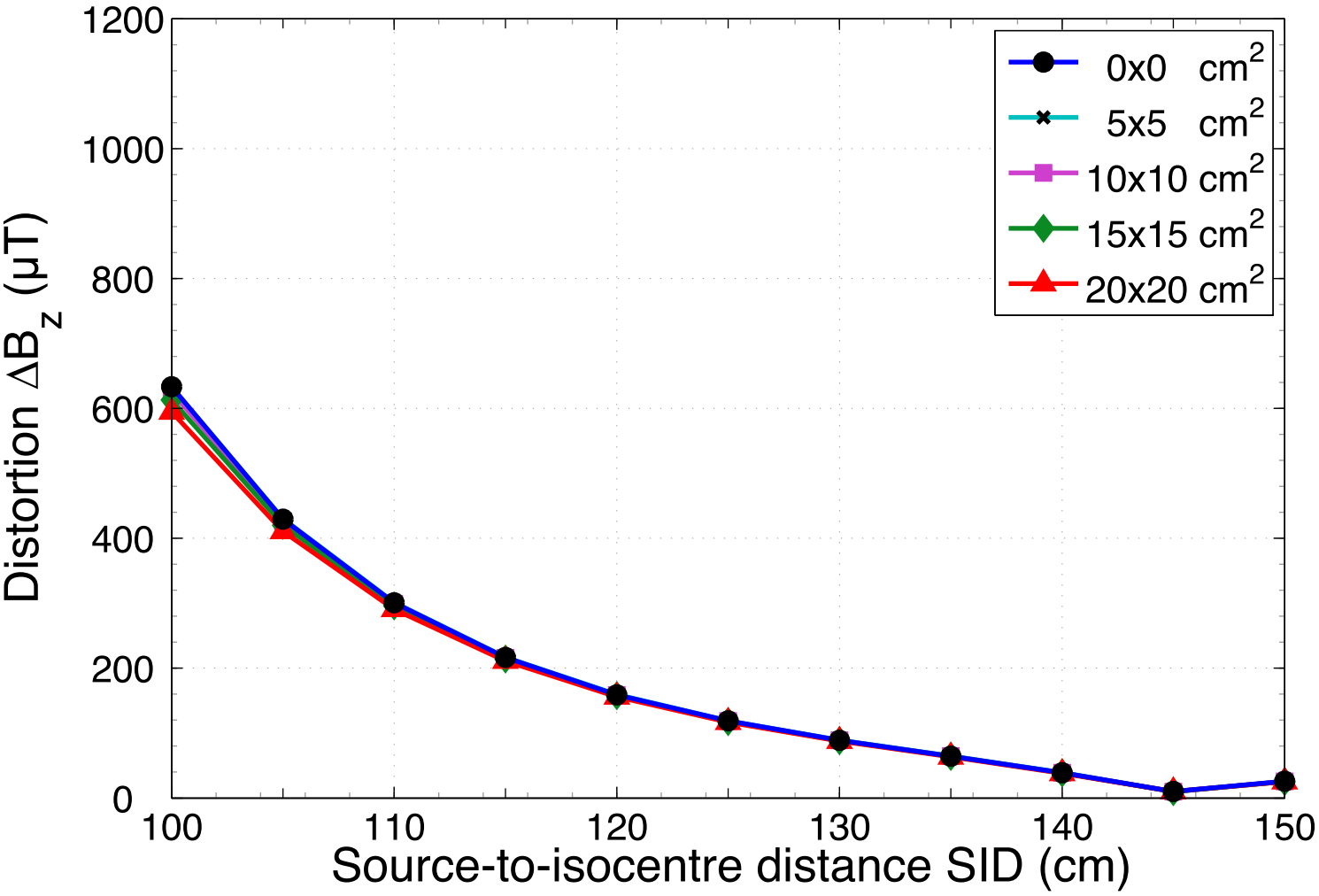
1200
1000
800
600
400
200
0
Distortion ΔB_z (μT)
100
110
120
130
140
150
Source-to-isocentre distance SID (cm)
0x0 cm²
5x5 cm²
10x10 cm²
15x15 cm²
20x20 cm²

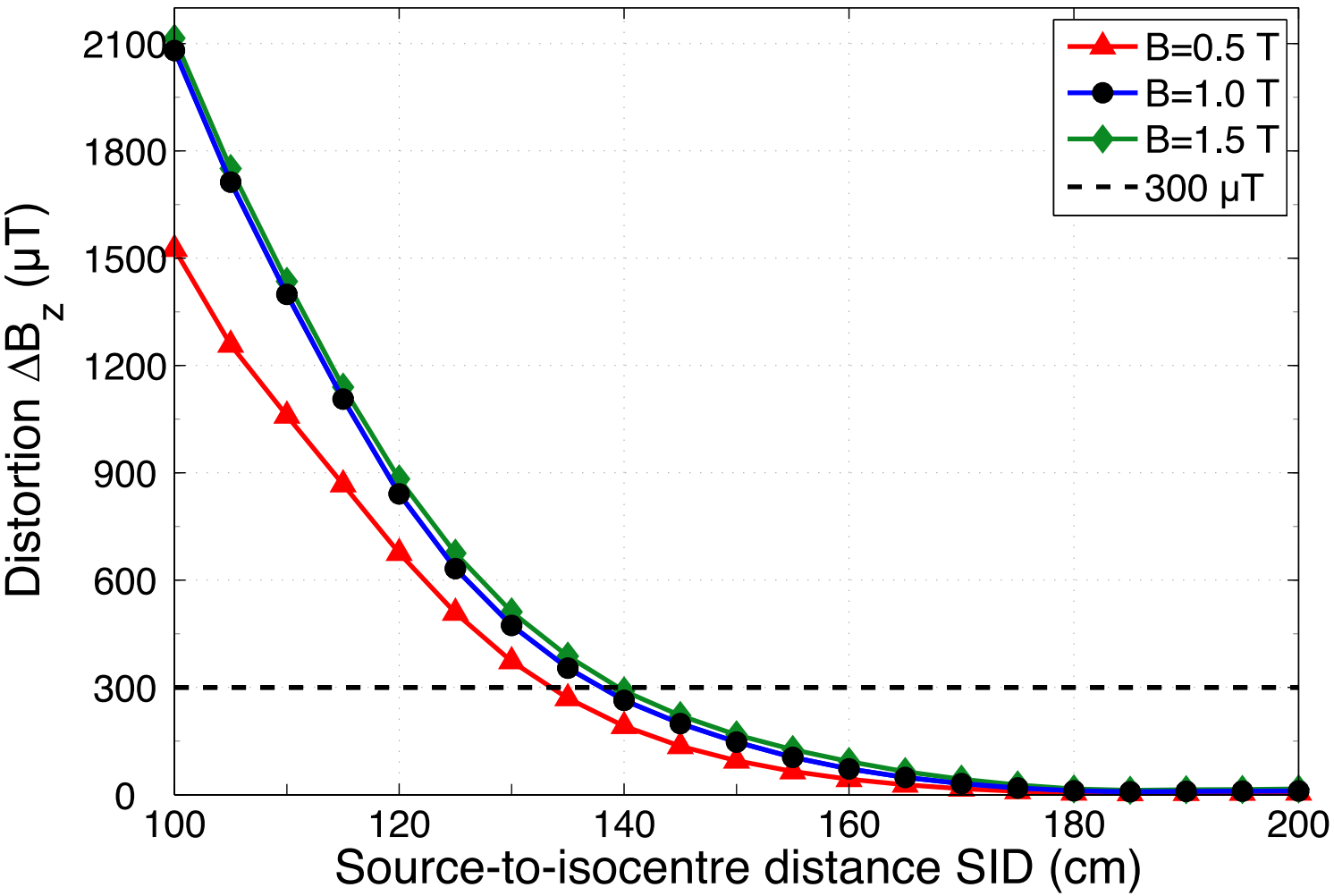
B=0.5 T
B=1.0 T
B=1.5 T
300 µT
Distortion ΔB_z (µT)
2100
1800
1500
1200
900
600
300
0
100
120
140
160
180
200
Source-to-isocentre distance SID (cm)

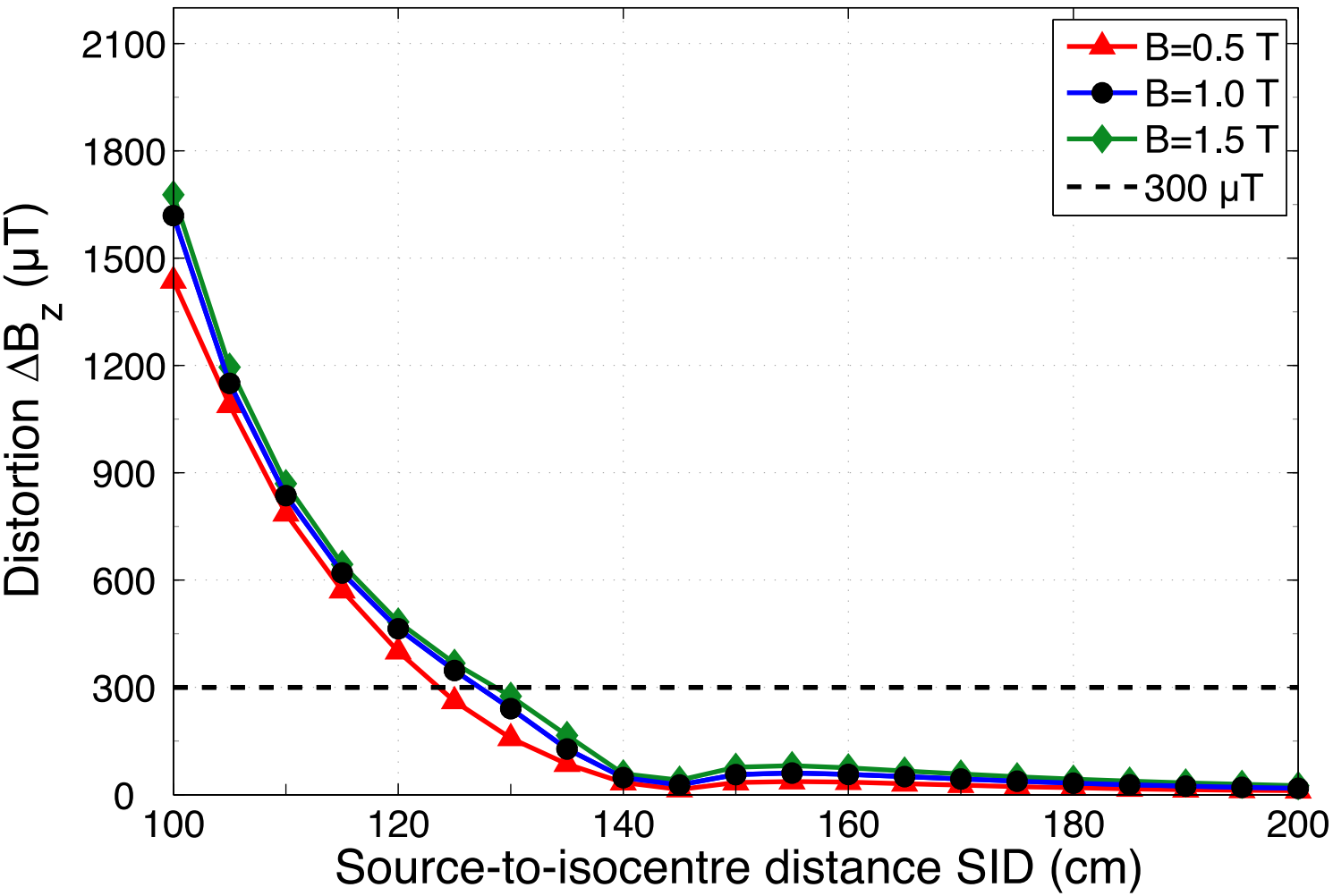
2100
1800
1500
1200
900
600
300
0
100
120
140
160
180
200
Distortion ΔB_z (μT)
Source-to-isocentre distance SID (cm)
B=0.5 T
B=1.0 T
B=1.5 T
300 μT